ผลของการเติมซีเรียมไดออกไซด์ที่มีต่อสมบัติและความว่องไวในการเร่งปฏิกิริยาแบบใช้แสงของตัวเร่งปฏิกิริยาซีเรียมไดออกไซด์/ไททาเนียมไดออกไซด์สำหรับปฏิกิริยาออกซิเดชันของเอทิลีนที่ใช้ตัวเร่งปฏิกิริยาแบบใช้แสง

นาย สืบสกุล โพธิ์เกษม

วิทยานิพนธ์นี้เป็นส่วนหนึ่งของการศึกษาตามหลักสูตรปริญญาวิศวกรรมศาสตรมหาบัณฑิต

สาขาวิชาวิศวกรรมเคมี ภาควิชาวิศวกรรมเคมี

คณะวิศวกรรมศาสตร์ จุฬาลงกรณ์มหาวิทยาลัย

ปีการศึกษา 2548

ISBN 974-53-1528-1

EFFECTS OF CERIUM DIOXIDE ADDITION ON THE PROPERTIES AND PHOTOCATALYTIC ACTIVITIES OF CeO_2/TiO_2 CATALYSTS FOR PHOTOCATALYTIC OXIDATION OF ETHYLENE

Mr. Seubsakul Pokasem

A Thesis Submitted in Partial Fulfillment of the Requirements
for the Degree of Master of Engineering in Chemical Engineering
Department of Chemical Engineering
Faculty of Engineering
Chulalongkorn University
Academic Year 2005
ISBN 974-53–1528-1

Thesis Title	EFFECTS OF CERIUM DIOXIDE ADDITION ON THE PROPERTIES AND PHOTOCATALYTIC ACTIVITIES OF CeO_2/TiO_2 CATALYSTS FOR PHOTOCATALYTIC OXIDATION OF ETHYLENE
By	Mr. Seubsakul Pokasem
Field of Study	Chemical Engineering
Thesis Advisor	Akawat Sirisuk, Ph.D.

Accepted by the Faculty of Engineering, Chulalongkorn University in Partial Fulfillment of the Requirements for the Master's Degree

....Dean of the Faculty of Engineering

(Professor Direk Lavansiri, Ph.D.)

THESIS COMMITTEE

.....Chairman

(Professor Piyasan Praserthdam, Dr.Ing.)

..... Thesis Advisor

(Akawat Sirisuk, Ph.D.)

..... Member

(Assistant Professor Joongjai Panpranot, Ph.D.)

.....Member

(Assistant Professor Seeroong Prichanont, Ph.D.)

สืบสกุล โพธิ์เกษม : ผลของการเติมซีเรียมไดออกไซด์ที่มีต่อสมบัติและความว่องไวในการเร่งปฏิกิริยาแบบใช้แสงของตัวเร่งปฏิกิริยาซีเรียมไดออกไซด์/ไทเทเนียมไดออกไซด์สำหรับปฏิกิริยาออกซิเดชันของเอทิลีนที่ใช้ตัวเร่งปฏิกิริยาแบบใช้แสง (EFFECTS OF CERIUM DIOXIDE ADDITION ON THE PROPERTIES AND PHOTOCATALYTIC ACTIVITIES OF CeO_2/TiO_2 CATALYSTS FOR PHOTOCATALYTIC OXIDATION OF ETHYLENE) อ. ที่ปรึกษา: ดร.อัครวัต ศิริสุข, 90 หน้า, ISBN: 974–53–1528-1

ตัวเร่งปฏิกิริยาซีเรีย/ไททาเนียสามารถเตรียมได้โดยวิธีโซลเจลและถูกนำไปเผาภายใต้อุณหภูมิ 300 °C เป็นเวลา 2 ชั่วโมง ของผสมโลหะออกไซด์มีปริมาณของซีเรียซึ่งอยู่ในช่วง 0-10% โดยโมล การทดสอบสมบัติของตัวเร่งปฏิกิริยาซีเรีย/ไททาเนียนั้น ทำโดยใช้การกระเจิงของรังสีเอ็กซ์ ความสามารถในการดูดซับก๊าซไนโตรเจนบนพื้นผิวตัวเร่งปฏิกิริยา ยูวีวิสซิเบิลแอปซอร์พชันสเปคโตรสโคปี (UV-Vis) อิเล็คตรอนสปินเรโซแนนซ์ (ESR) อินดัคทีฟคูเปิลพลาสมาอะตอมมิคอิมิชชันสเปคโตรสโคปี (ICP) ฟูเรียทรานซฟอร์มอินฟราเรดสเปคโตรสโคปี (FT-IR) และเอ็กซ์เรย์โฟโต้อิเล็คตรอนสเปคโตรสโคปี (XPS) ความสามารถในการเร่งปฏิกิริยาเชิงแสงของตัวเร่งปฏิกิริยาซีเรีย/ไททาเนียถูกทดสอบในปฏิกิริยาการสลายตัวของเอทิลีนภายใต้การฉายแสงอัลตราไวโอเลต จากผลการทดลองแสดงให้เห็นว่าความว่องไวของการเกิดปฏิกิริยาของตัวเร่งปฏิกิริยาซีเรีย/ไททาเนียจะลดลงอย่างมากตามปริมาณของซีเรียที่เพิ่มขึ้น ซึ่งมีสาเหตุมาจากปริมาณของ Ti^{3+} บนพื้นผิวของตัวเร่งปฏิกิริยาลดน้อยลง พลังงานระหว่างแถบชั้นพลังงานลดต่ำลง รวมทั้งปริมาณของหมู่ไฮดรอกซิลบนพื้นผิวของตัวเร่งปฏิกิริยาก็ลดต่ำลงด้วย อย่างไรก็ตามเมื่อนำตัวเร่งปฏิกิริยาซีเรีย/ไททาเนียมาทดสอบกับสารตั้งต้นประเภทแอลกอฮอล์อย่างเช่นเมทานอลและไอโซโพรพานอล กลับพบว่าปริมาณของซีเรียที่ใส่ลงไปในโลหะออกไซด์ผสมที่ให้ผลดีที่สุดคือที่ 0.5% โดยโมล ที่เป็นเช่นนี้อาจเกิดจากเส้นทางการเกิดปฏิกิริยาที่ต่างกัน

ภาควิชา.... ...วิศวกรรมเคมี..... ลายมือชื่อนิสิต.....สืบสกุล โพธิ์เกษม.....

สาขาวิชา.....วิศวกรรมเคมี..... ลายมือชื่ออาจารย์ที่ปรึกษา.....

ปีการศึกษา.....2548.....

##4770500721: MAJOR CHEMICAL ENGINEERING
KEY WORD: TITANIUM (IV) OXIDE / SOL-GEL METHOD / CERIUM (IV) OXIDE / PHOTOCATALYTIC OXIDATION OF ETHYLENE

SEUBSAKUL POKASEM: EFFECTS OF CERIUM DIOXIDE ADDITION ON THE PROPERTIES AND PHOTOCATALYTIC ACTIVITIES OF CeO_2/TiO_2 CATALYSTS FOR PHOTOCATALYTIC OXIDATION OF ETHYLENE THESIS ADVISOR: AKAWAT SIRISUK, Ph.D. 90 pp. ISBN 974-53-1528-1

A series of cerium dioxide/titanium dioxide (CeO_2/TiO_2) photocatalysts were prepared via a sol-gel method and were calcined at 300 °C for 2 hr. A mixed oxide consisted of TiO_2 as the major phase and CeO_2 as the dopant phase in the range of 0-10% mol. Properties of ceria-titania mixed oxides have been investigated using X-ray diffraction (XRD), nitrogen physisorption, inductively coupled plasma atomic emission spectroscopy, UV-Visible absorption spectroscopy, electron spin resonance, fourier transform infrared spectroscopy, and X-ray photoelectron spectroscopy (XPS). The photocatalytic activities of CeO_2/TiO_2 catalysts were evaluated for the degradation of ethylene under UV illumination. The experimental results demonstrated that the photocatalytic activities of CeO_2/TiO_2 catalysts dramatically decreased with increasing ceria content. This decrease was due to the smaller amount of Ti^{3+} surface defects, smaller band-gap energy, and fewer hydroxyl groups on the catalyst surface. However, when alcohol (i.e., methanol and 2-propanol) was employed as a reactant, we obtained the highest photocatalytic activity for the oxidation of alcohol with the mixed oxide catalyst that contained 0.5% mole of ceria. This result can be explained by different reaction pathways.

Department.....Chemical Engineering..... Student's signature.....Seubsakul Pokasem
Field of study....Chemical Engineering..... Advisor's signature.....
Academic year.....2005.....

ACKNOWLEDGEMENTS

This dissertation would not have been possible to complete without the support of the following individuals. Firstly, I would like to express my greatest gratitude to my advisor, Dr. Akawat Sirisuk, for his invaluable guidance during the course of this work, and I am also very grateful to Professor Dr. Piyasan Praserthdam, for his kind supervision over this thesis as the chairman, Assistant Professor Joongjai Panpranot and Assistant Professor Seeroong Prichanont, members of the thesis committee for their kind cooperation.

The financial supports from the Graduate School of Chulalongkorn University are also gratefully acknowledged.

Many thanks for kind suggestions and useful help to Mr. Kongkiat Suriye and many friends in the Research Center on Catalysis and Catalytic Reaction Engineering who always provide the encouragement and assistance along the thesis study.

Finally, I also would like to dedicate this thesis to my parents, my aunt and my sister who have always been the source of my support and encouragement.

CONTENTS

	Page
ABSTRACT (IN THAI).....	iv
ABSTRACT (IN ENGLISH).....	v
ACKNOWLAGEMENTS.....	vi
CONTENTS.....	vii
LIST OF TABLES…….....	xi
LIST OF FIGURES…….....	xii
CHAPTER	
I INTRODUCTION…….....	1
II LITERATURE REVIEWS.....	5
2.1 Effects of ceria added to CeO_2/TiO_2 mixed oxides on properties and photocatalytic activities..……	5
III THEORY.....	9
3.1 Photocatalytic process……..…….....	9
3.2 Sol-gel method…….	12
3.3 Materials employed as photocatalysts……..	13
3.1.1 Titanium dioxide…….....	14
3.1.1.1 Physical and chemical properties…….....	14
3.1.1.2 Applications of titanium dioxide.....	17
3.1.2 Cerium dioxide …….....	19
3.1.2.1 Physical and chemical properties……	19
3.1.2.2 Applications of cerium dioxide……...…….	19
IV EXPERIMENTAL.....	21
4.1 Catalyst preparation……..…….....	21
4.1.1 Preparation of TiO_2 and CeO_2/TiO_2 nanoparticles……...	21
4.2 Catalyst characterization……..	22
4.2.1 X-ray Diffractometry (XRD).....	22
4.2.2 Nitrogen Physisorption (BET)…….	24
4.2.3 Electron Spin Resonance Spectroscopy (ESR).....	24
4.2.4 Fourier Transform Infrared Spectroscopy (FT-IR)……..	24

Page

4.2.5 Inductively Coupled Plasma Atomic Emission Spectroscopy (ICP-AES)…… 24
4.2.6 UV-Vis Absorption Spectroscopy (UV-Vis)..... 25
4.2.7 X-ray Photoelectron Spectroscopy (XPS)..... 25
4.3 Photocatalytic activity measurements for the catalysts…… 25
4.3.1 Apparatus..... 26
4.3.1.1 Photoreactor..... 26
4.3.1.2 Gas Controlling System…..... 27
4.3.2 Experimental procedure for determining the activity of the photocatalyst..... 27
4.3.2.1 Photocatalytic oxidation of ethylene in gas phase reaction……... 27
4.3.2.2 Photocatalytic oxidation of 2-propanol in gas and liquid phases…….. 29
4.3.2.3 Photocatalytic oxidation of methanol, acetone and benzene in gas phase reaction……... 31
V RESULTS AND DISSCUSSION……..... 33
5.1 Characterization of the catalysts..... 33
5.1.1 Determination of composition content..... 33
5.1.2 Specific surface area measurement..... 33
5.1.3 Crystal structure……... 34
5.1.4 Fourier Transform Infrared Spectroscopy (FT-IR)…….. 37
5.1.5 UV-Vis Absorption Spectroscopy (UV-Vis)..... 38
5.1.6 Electron Spin Resonance (ESR)…….. 39
5.1.7 X-ray Photoelectron Spectroscopy (XPS)…… 41
5.2 Photocatalytic activity testing 44
5.2.1 Effect of cerium loading in CeO_2/TiO_2 mixed oxides on the photocatalytic oxidation of ethylene…….. 44
5.2.2 Effect of flowrate on the activities of CeO_2/TiO_2 mixed oxides in the photocatalytic oxidation of ethylene……... 47

Page

5.2.3 Effect of humidity on the activities of CeO_2/TiO_2 mixed oxides in ethylene photooxidation……... 48
5.3 Photocatalytic oxidation of other organic compounds over CeO_2/TiO_2 mixed oxides …….. 49
5.4 Comparison of photocatalytic oxidation of 2-propanol in gas and liquid phases for CeO_2/TiO_2 mixed oxides ……..... 57
VI CONCLUSIONS AND RECOMMENDATIONS..... 59
6.1 Conclusions..... 59
6.2 Recommendations for future studies..... 60
REFERENCES..... 61
APPENDICES..... 65
APPENDIX A: CALCULATION OF THE CRYSTALLITE SIZE..... 66
APPENDIX B: THE OPERATING CONDITIONS OF GAS CHROMATOGRAPHY..... 69
APPENDIX C: THE CHARACTERISTIC OF REACTANTS TESTED IN THE PHOTOCATALYTIC OXIDATION……... 71
APPENDIX D: CALCULATION OF VAPOR PRESSURE OF SUBSTANCE……..... 81
APPENDIX E: DETERMINATION OF Ti^{3+} SURFACE DEFECT FROM ESR MEASUREMENT……. 82
APPENDIX F: DETERMINATION OF LATTICE PARAMETERS OF TITANIUM DIOXIDE…... 83
APPENDIX G: POSITION OF TITANIUM OXIDATION STATE…… 86
VITA..... 88

LIST OF TABLES

Table **Page**

3.1 Comparison of properties of rutile, brookite and anatase……... 14

3.2 Selected physicochemical properties of cerium dioxide …..... 19

4.1 Operating conditions for gas chromatography GC-14B……. 29

4.2 Operating conditions for gas chromatography GC-8A..……. 30

4.3 Operating conditions for gas chromatography GC-9A..……. 32

5.1 specific surface area and Ce:Ti mol ratios of various CeO_2/TiO_2 mixed oxides calcined at 300 ^oC for two hours..…… 34

5.2 Specific surface areas and crystallite sizes of various CeO_2/TiO_2 mixed oxides calcined at 300 ^oC for two hours……. 36

5.3 The amount of Ti^{3+} surface defects of TiO_2 and CeO_2/TiO_2 mixed oxide catalysts calcined at 300 °C for two hours from ESR measurements…… 41

5.4 XPS binding energy values for TiO_2 and various CeO_2/TiO_2 samples after calcinations at 300 ^oC for two hours……... 42

5.5 XPS core-level binding energies (eV) and XPS peak areas for TiO_2 and CeO_2/TiO_2 catalysts calcined at 300 ^oC for two hours after etching…….. 44

5.6 Bond energy of ethylene, acetone and benzene…….. 55

B.1 The operating condition for gas chromatograph..... 69

C.1 The specific and thermodynamic properties of ethylene…… 72

C.2 The specific and thermodynamic properties of methanol…….. 74

C.3 The specific and thermodynamic properties of acetone……. 76

C.4 The specific and thermodynamic properties of isopropanol…….. 78

C.5 The specific and thermodynamic properties of benzene…… 79

D.1 The vapor pressure of chemicals at 30^oC by Antoine equation……. 81

E.1 The amount of Ti^{3+} surface defects of TiO_2 and CeO_2/TiO_2 mixed oxide catalysts calcined at 300 °C for two hours…… 82

F.1 The 2θ value of (101) plane and (200) plane of TiO_2 in each sample from XRD measurement…… 84

F.2 Summary of lattice parameter and crystal volume from XRD analysis……. 85

G.1 The list of binding energy position and reference of each element……... 87

LIST OF FIGURES

Figure **Page**

3.1 Photocatalytic process occurring on an illuminated semiconductor particle.. 10

3.2 surface and bulk electron trapping…….. 11

3.3 Energy diagram for TiO_2 and relevant redox potentials……. 15

3.4 Crystal structure of anatase (left-hand) and rutile (right-hand) TiO_2……. 16

3.5 application chart of titanium dioxide…….. 18

4.1 Schematic diagram for the preparation method of TiO_2 and CeO_2/TiO_2 samples by sol-gel synthesis……... 23

4.2 Photoreactor set for experiments……. 26

4.3 Flow diagram of heterogeneous photocatalytic oxidation (PCO)……... 28

5.1 XRD patterns of CeO_2/TiO_2 mixed oxides calcined at 300 ^oC for 2 hr; (a) pure TiO_2, (b) 0.1 mol%, (c) 0.5 mol%, (d) 1 mol%, (e) 2 mol%, (f) 5 mol%, (g) 10 mol% CeO_2/TiO_2 catalysts……..... 35

5.2 FT-IR spectra of various CeO_2/TiO_2 mixed oxides calcined at 300 ^oC for two hours; (a) pure TiO_2, (b) 0.1 mol%, (c) 0.5 mol%, (d) 1 mol%, (e) 2 mol%, (f) 5 mol% and (g) 10 mol% CeO_2/TiO_2 catalysts…….. 37

5.3 The UV-vis diffuse reflectance spectra of TiO_2 and CeO_2/TiO_2 mixed oxide catalysts calcined at 300 ^oC for two hours…… 38

5.4 ESR spectra of CeO_2/TiO_2 mixed oxides calcined at 300 ^oC for two hours; (a) pure TiO_2, (b) 0.1 mol%, (c) 0.5 mol%, (d) 1 mol%, (e) 2 mol%, (f) 5 mol%, (g) 10 mol% CeO_2/TiO_2 catalysts. The amount of Ti^{3+} surface defect was related to peak height. The g-value of Ti^{3+} defect was at 1.998... 40

5.5 Typical XPS O 1s and Ti 2p spectra for 10% mole CeO_2/TiO_2 sample calcined at 300 ^oC for two hours……. 43

5.6 Influence of cerium content on the activities of CeO_2/TiO_2 mixed oxides for photocatalytic oxidation of ethylene. The flowrate of 0.001% vol ethylene in air was 15 ml min^{-1} and 0.2 g of photocatalyst was used……. 45

Figure **Page**

5.7 Effect of flow rate of reactant on the photocatalytic activities of CeO_2/TiO_2 catalyst for photocatalytic oxidation of ethylene. Reaction time was 180 min and 0.2 g of catalyst was used…….. 47

5.8 Effect of humidity on the activities of CeO_2/TiO_2 mixed oxide for photocatalytic oxidation of ethylene. The reactant gas flowed through 0.2 g of catalyst at a flow rate of 15 ml min^{-1}. Reaction time was 180 minutes. 48

5.9 Conversion as a function of cerium loading for photocatalytic oxidation of ethylene, acetone and benzene. The reactant gas flowed through 0.2 g of catalyst at a flow rate of 5 ml min^{-1}. Reaction time was 180 minutes……... 50

5.10 Conversion as a function of cerium loading for photocatalytic oxidation of methanol and 2-propanol. The reactant gas flowed through 0.2 g of catalyst at a flow rate of 5 ml min^{-1}. Reaction time was 180 minutes……... 51

5.11 Effect of cerium addition on Ti^{3+} surface sites and ceria sites..... 56

5.12 Conversion as a function of cerium loading for photocatalytic oxidation of 2-propanol over CeO_2/TiO_2 catalysts in gas and liquid phases. Reaction time was three hours…… 58

A.1 The 101 diffraction peak of titania for calculation of the crystallite size….. 67

A.2 The plot indicating the value of line broadening due to the equipment. The data were obtained by using α-alumina as standard…….. 68

B.1 The calibration curve of ethylene..... 70

C.1 The structural formula of ethylene……. 71

C.2 The structural formula of methanol…… 73

C.3 The structural formula of acetone…….. 76

C.4 The structural formula of isopropanol…… 77

C.5 The structural formula of benzene…….. 79

F.1 Tetragonal crystal structure of titanium dioxide……. 83

G.1 The binding energy and area of each Ti oxidation state…… 86

CHAPTER I

INTRODUCTION

Volatile organic compounds (VOCs) are widespread pollutants originated by either industrial or domestic sources (Hester et al., 1995). Many of them are known to be noxious and/or carcinogenic and consequently there is a considerable concern about the consequences of exposing the population of these substances. In order to limit these risks for the health, several methods for the removal of these compounds have been proposed. Among them, heterogeneous photocatalytic oxidation (PCO) constitutes a promising technique for the degradation of volatile organic compounds (Maira et al., 2001) because of its capability of eradicating a variety of chemicals under mild condition in the presence of a semiconductor photocatalyst (e.g., TiO_2) and UV or near-UV light source (Peral and Ollis., 1992; Hoffman et al., 1995). The photocatalytic oxidation using TiO_2 photocatalyst has been studied by several researchers (Sirisuk et al., 1999; Fu et al., 1996; Park et al., 1999) who observed different catalyst activities and efficiencies for TiO_2 that was prepared differently.

Titanium dioxide (TiO_2) is one of the most popular and promising materials in photocatalytic application due to its strong oxidizing power of its holes, high photostability and redox selectivity (Ohtani et al., 1997). TiO_2 is commercially available and is easy to prepare in the laboratory. In addition, undoped TiO_2 has a band gap of 3.2 eV, which allows titania to absorb lights with wavelengths shorter than 385 nm. In recent years, researchers have synthesized a variety of nanosized TiO_2 materials as nano-particles, nano-wires and so on. Titania has three naturally occurring polymorphs, namely, anatase, brookite, and rutile. Despite the criticisms of Liu and Merragh (Liu et al., 1992) rutile have been considered the most stable polymorph at standard conditions. Anatase and brookite are considered as kinetic products, despite the fact that depending on the particle size, anatase becomes more stable than rutile (Liu et al., 1992). It has been shown that the previous treatment of the synthesized titania powders exerts remarkable effects on its properties as well as on the structural transitions observed under heating (Zhang et al., 1998; Ovenstone et

al., 1999; Yanagizawa et al., 1998). Photocatalytic activity of TiO_2 catalysts depends strongly on two factors: adsorption behavior and the separation efficiency of electron-hole pairs (Fujishima et al., 2000; Kamat, 1993; Hoffman et al., 1995). The adsorption capacity can be generally improved by adjusting the surface zero-charge point or by increasing the specific surface area and pore volume of catalysts (Li et al., 2001; Yu et al., 2003; Cheng et al., 2003).

However, the most active photocatalyst, anatase form of titanium dioxide (TiO_2), presents a moderate yield and the total oxidation of certain substrates is not easily achieved. Formation of a substantial amount of partially oxidized products is another issue that has to be mentioned when oxidizing certain pollutants, like toluene and xylene (Augugliaro et al., 1999). In addition, partial deactivation of catalyst is occasionally observed, especially with photocatalytic oxidation of aromatic substances (Augugliaro et al., 1999; Alberici and Jardim., 1995). In order to overcome these difficulties, several modifications of the photocatalysts have been proposed. Careful control of the nanoscale structure of the TiO_2 samples leads to a considerable improvement of their PCO performance (Maira et al., 2000; Maira et al., 2001). Furthermore, incorporation of noble metals like platinum to the photocatalysts can also result in an increase in the reaction rate, most likely due to the stabilization of the photoproduced charge carriers (Fu et al., 1995). Insertion of transition metal ions on the titania structure can significantly enhance the photonic efficiency, either by widening the light absorption range or by modifying the redox potential of the photoproduced radicals (Hoffman et al., 1995; Lin et al., 1999; Anpo., 2000). An alternative approach is establishing electronic contacts between different semiconductors (Hoffman et al., 1995; Tada et al., 2000). In many cases, a suitable choice of the materials brought into contact can enhance the photocatalytic activity by increasing the efficiency for charge separation (Tada et al., 2000).

One promising approach is the substitution of another metal or metal oxide in the titania lattice. Alternatively, photocatalytic activity of TiO_2 could be significantly enhanced by doping with lanthanide ions or oxides with 4*f* electron configurations because lanthanide ions could form complexes with various Lewis bases including organic acids, amines, aldehydes, alcohols, and thiols in the interaction of the functional groups with their *f*-orbital (Ranjit et al., 2001; Willner et al., 2001).

However, the effect of lanthanide oxides on the separation of electron-hole pairs under visible light irradiation and the photoresponse had seldom been investigated in these publications. Among the lanthanide oxides, ceria (CeO_2) have received enormous attention because of (i) the redox couple Ce^{3+}/Ce^{4+}, with the ability of ceria to shift between CeO_2 and Ce_2O_3 under oxidizing and reducing conditions, respectively, and (ii) the ease of formation of labile oxygen vacancies and the relative high mobility of bulk oxygen species (Reddy et al., 2002). CeO_2 is frequently incorporated to the formulation of oxidation catalysts because it shows a considerable performance for the catalytic combustion of hydrocarbons and carbon monoxide (Trovarelli, 1996). The formation and annihilation of oxygen vacancies in redox processes occurring on the surface of ceria containing samples is considered to play a crucial role on these oxidative reactions (Trovarelli, 1996). In addition, ceria is an n-type semiconductor with a bandgap of about 2.95 eV. These characteristics suggest that CeO_2 could be potentially used as a photocatalyst for the oxidation of organic pollutants.

Therefore, we focus on the study of effects of CeO_2 addition on the properties and photocatalytic activities of CeO_2/TiO_2 mixed oxides prepared via a sol–gel method. Photocatalytic oxidation is employed as a main model reaction to determine photocatalytic activity of these catalysts under UV irradiation. The main goal of this research is to investigate and understand the effects of various factors on the photocatalytic activities of CeO_2/TiO_2 mixed oxides at various ratios. The study included the effects of flowrate and humidity on the photocatalytic activities in photocatalytic oxidation of ethylene, the effect of different phases of reactant in photocatalytic oxidation of 2-propanol, and the different types of reactants on the photocatalytic activities in gas-phase reaction of CeO_2/TiO_2 mixed oxides. The reactants used in this study were ethylene, methanol, acetone, 2-propanol, and benzene.

The objectives of this research are as follows:

1. To learn how to prepare CeO_2/TiO_2 mixed oxides using a sol-gel method

2. To investigate effects of the amount of CeO_2 addition on properties and photocatalytic activities of CeO_2/TiO_2 mixed oxides

3. To investigate effects of the following parameters on properties and photocatalytic activity of CeO_2/TiO_2 mixed oxides calcined at 300 ^{o}C for 2 hr:

- amount of CeO_2 added
- flowrate and humidity
- phase of reaction
- the types of reactants in gas phase reaction

This thesis is arranged as follows:

Chapter I mentions the introduction of this work

Chapter II presents literature reviews of previous works related to this research.

Chapter III explains the principle of catalyst preparation via sol-gel method and basic information about titania and ceria such as physical properties as well as the principles of photocatalytic process.

Chapter IV describes synthesis of CeO_2/TiO_2 mixed oxides employed in this research, experimental apparatus and characterization equipments.

Chapter V describes experimental results and discussion of this research.

Chapter VI presents overall conclusions of this research and recommendations for future work.

CHAPTER II

LITERATURE REVIEWS

This chapter contains a survey of several studies involving ceria/titania mixed oxide photocatalysts prepared via various methods. This section discusses the effects of ceria addition to titania photocatalyst on properties of catalysts changed like radicals, surface oxygen vacancy, phase transformation of titania, etc. including photocatalytic activity on photocatalytic oxidation of hydrocarbons.

2.1 Effects of ceria added to CeO_2/TiO_2 mixed oxides on properties and photocatalytic activities

Li and coworkers (2005) found that the photocatalytic activity of TiO_2 could be significantly enhanced by doping with lanthanide ions/oxides because lanthanide ions could form complexes with various Lewis bases including organic acids, amines, aldehydes, alcohols, and thiols in the interaction of the functional groups with their *f*-orbitals. Crystal structure of a series of Ce^{3+}-TiO_2 catalysts with various contents of Ce^{3+} had similar XRD patterns dominated by anatase phase. The relative intensity of the main anatase peak (1 0 1) decreased with the increase of Ce^{3+} content. This decrease might indicate that the doping of cerium ion inhibited the phase transformation from amorphous TiO_2 to anatase, and that Ce^{3+}-TiO_2 had higher thermal stability than pure TiO_2. The overall photocatalytic activity for 2-mercaptobenzothiazole degradation under UV or visible light irradiation was signficiantly enhanced by doping with cerium ions with a special 4*f* electron configuration because of larger adsorption equilibrium constant and greater separation efficiency of electron-hole pairs for Ce^{3+}-TiO_2 catalysts. The introduction of 4*f* orbitals of cerium led to the optical absorption band between 400 and 500 nm. The formation of two sub-energy levels (defect level and 4*f* level) in Ce^{3+}-TiO_2 may be attributed to suppression of the recombination of electron-hole pairs and enhancement of the photocatalytic activity under UV or visible light illumination. In addition, the higher content of Ti^{3+} on the Ce^{3+}-TiO_2 surface compared to that of TiO_2 would

accelerate the interfacial charge transfer and enhance the photocatalytic activity. However, the content of Ti^{3+} should have an optimal range. In the study, it was found that the Ti^{3+} content increased with the increase of Ce^{3+} dosage. The defect level would become the recombination center of electron-hole pairs and led to the decrease of photocatalytic activity when Ti^{3+} content exceeded its optimal value. The optimal dosage of cerium ion under visible light illumination was found to be 0.7%, while that under UV illumination was 1.2%.

Liu and coworkers (2005) reported that cerium oxide (CeO_{2-y}, $0<y<0.5$, 3–7 wt% Ce) could be incorporated into TiO_2 via an in situ sol-gel process. This solution-based reaction led to a uniform distribution of cerium oxide in TiO_2 matrix and also produced nanosized mixed oxide spheres. When fired at a temperature below 600 ^oC, the anatase TiO_2 grew with increasing temperature regardless of whether TiO_2 was doped or not. However, at a higher firing temperature ranging from 600 to 800^oC, the transformation from anatase to rutile phase was hindered in the CeO_{2-y}–TiO_2 mixed oxide. The XRD pattern of CeO_{2-y} phase was observed in this temperature range. The light absorbance of CeO_{2-y}–TiO_2 shifted to the wavelength range of 380-460 nm and the intensity of absorbance was apparently affected by the content of CeO_{2-y}. The doping of 5 wt% CeO_{2-y} gave the maximum absorption in the above range. Coincidently, the electrical conductivity of CeO_{2-y}–TiO_2 mixed oxide was found to increase with increasing CeO_{2-y} content. This increase was an indicative of formation of n-type doping structure, that allowed the oxide absorb light with longer wavelengths.

De Farias and Airoldi (2005) have studied the stabilization of anatase phase at high temperatures of sol–gel cerium and copper doped titania and titania–silica powders. Cerium-doped titania samples remained as anatase phase until calcination temperature exceeded 800 ^oC, whereas copper-doped samples calcined at the same temperature contained a mixture of anatase and rutile phases.

Sinha and Suzuki (2005) have studied mesoporous ceria-titania that contained different Ce/Ti ratios (1:2, 1:1, 2:3). The mixed oxides had large specific surface areas with narrow pore size distributions in the mesoporous range after calcination at 700

°C. The materials showed high activities for removal of ethylene at room temperature, compared to nonporous ceria-titania, mesoporous ceria, and mesoporous titania.

Sinha and Suzuki (2005) have studied the preparation and characterization of novel mesoporous ceria-titania with different Ce/Ti ratios (0.5:1, 1:1, 1:1.5) prepared by a neutral templating route. The obtained material had thermal stability and high surface areas with a narrow pore size distribution in the mesoporous range after calcination up to 973 K. UV-vis and XPS analysis indicated the presence of well-dispersed ceria and titania components with negligible bulk oxide formation. The material showed high VOC removal ability in the total oxidation of toluene in air at room temperature compared to nonporous ceria-titania, mesoporous ceria and mesoporous titania. The toluene removal ability almost doubled after Pt impregnation on mesoporous ceria-titania, most likely because of the synergetic effect between the Pt sites and the metal oxide sites. These results suggest that mesoporous ceria-titania mixed oxides are very promising for air-purification applications.

Coronado and coworkers (2002) studied the radicals formed upon UV irradiation of ceria-based photocatalysts. They found that TiO_2, CeO_2/TiO_2 and CeO_2 materials are shown to present activity for toluene photocatalytic oxidation, although the maximum degradation rate belonged to the pure anatase sample. In the case of the CeO_2/TiO_2 catalyst, EPR results indicated that photoactivation occured on both components. Experimental results indicated that the main effect of ceria incorporation to the titania sample was the partial blockage of the surface sites available for toluene photodegradation. In the case of CeO_2, the oxidation rate was one order of magnitude lower than those of the TiO_2-based materials. This behavior, along with the temperature dependence of the activity, indicated that photo-oxidation took place according to a different mechanism on CeO_2. The EPR study of the CeO_2 sample showed that UV illumination in the presence of oxygen induced the formation of O_2^- and other radicals, which were derived from trapping of photogenerated electrons. These species may play a role in the photodegradation process, although the lower width of the bandgap interval implied a lower oxidative potential of the holes photoproduced on CeO_2 compared to those formed on anatase. In these conditions, the

main effect of UV photoactivation of CeO_2 could favor the formation of surface oxygen vacancies.

The photocatalytic activities of the mixtures of TiO_2 (P25) with three rare earth oxides, namely, Y_2O_3, La_2O_3, and CeO_2, were studied by Lin and Yu (1998). Mixtures of TiO_2 with La_2O_3 (0.5 wt.%) or Y_2O_3 (0.5 wt.%) that were calcined at 650 °C or 700 °C exhibited higher photoactivities than pure TiO_2 for the oxidation of acetone. However, mixtures of TiO_2 with CeO_2 displayed lower photoactivity than pure TiO_2. The presence of these rare earth oxides inhibited transformation from anatase to rutile at elevated temperatures. The lower photocatalytic activity of TiO_2-CeO_2 mixtures was due to fast recombination rate of photogenerated electron-hole pairs and high isoelectric point in terms of pH value. Lower isoelectric point led to more hydroxide ions on the surface of catalyst. Consequently, hydroxide ions acting as hole traps that prevented electron-hole recombination and gave rise to high photoactivity.

CHAPTER III

THEORY

Heterogeneous photocatalysis has been extensively studied for decontamination of air and water polluted by VOCs. Using TiO_2 as a catalyst appears to be a promising process. In this chapter, photocatalytic process is described in section 3.1. In addition, detail about synthesis of such materials by sol-gel method is described in Section 3.2. And in the last section, materials to be used as photocatalysts, namely, titania and ceria, are discussed in section 3.3.

3.1 Photocatalytic process (Fujishima et al., 1999)

The primary photocatalytic process occurs upon irradiation of a semiconductor. A semiconductor has an electronic band structure. The highest occupied energy band (valence band) and the lowest empty band (conduction band) are separated by a band gap. The magnitude of the energy of band gap between the electronically populated valence band and the largely vacant conduction band governs the extent of thermal population of the conduction band in its intrinsic state. The band gap defines the wavelength sensitivity of the semiconductor to irradiation (Fox and Dulay, 1993).

A photon of energy higher than or equal to the band gap energy is absorbed by a semiconductor particle. Then an electron from the valence band is promoted to the conduction band with simultaneous generation of an electronic vacancy or "hole" (h^+) in the valence band. This process is photoexcitation of electrons. Figure 3.1 shows the photocatalytic process occurring on an irradiated semiconductor particle.

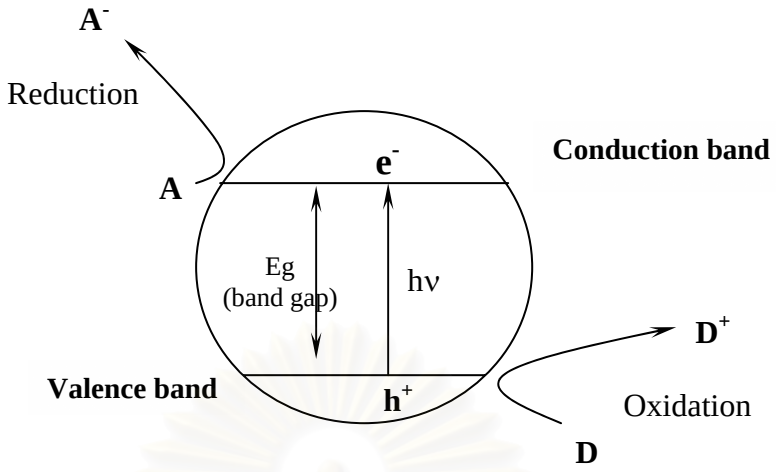

Figure 3.1 Photocatalytic process occurring on an illuminated semiconductor particle (Litter, 1999)

In most materials that are electrically conductive, i.e., metals, two types of charge carriers, electrons (e^-) and holes (h^+), immediately recombine on the surface or the bulk of particle in a few nanoseconds and the accompanying energy is dissipated as heat (see Equation 3.1). On semiconductor such as titanium dioxide, however, the charge carriers survive for longer periods of time. These carriers can be trapped in surface states, where they can react with donor (D) or acceptor (A) species adsorbed or close to the surface of the particle (Equations 3.2, 3.3, and 3.4) (Litter, 1999). Subsequently, oxidation and reduction can be initiated.

Recombination $$h^+ + e^- \rightarrow heat \quad (3.1)$$

Photoexcitation $$Semiconductor + h\nu \rightarrow e^- + h^+ \quad (3.2)$$

$$h^+ + D \rightarrow D^+ \quad (3.3)$$

$$e^- + A \rightarrow A^- \quad (3.4)$$

Electron-hole recombination processes may be suppressed by bulk and surface traps. In Figure 3.2, the energy levels of the bulk and surface traps fall within the band gap. The surface and bulk traps are localized, and the electrons trapped in such states are thus associated with a particular site on the surface or in the bulk of the solid. The population of bulk and surface traps depend on two factors, namely, the

decrease in entropy that occurs when electrons are trapped, and the difference in relative energy between the traps and the bottom of the conduction band.

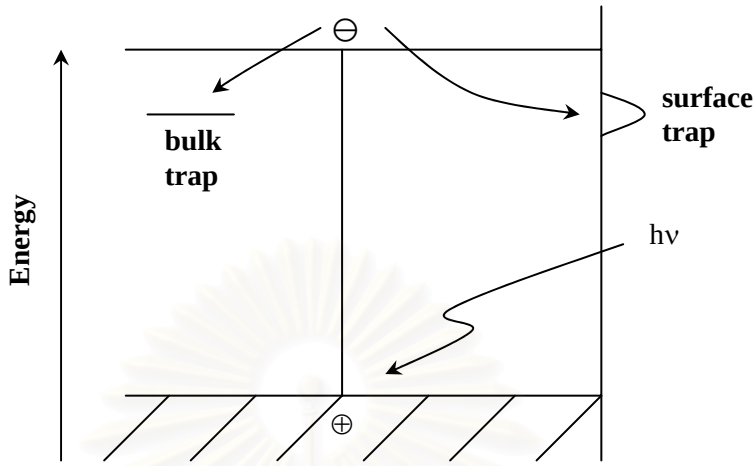

Figure 3.2 Surface and bulk electron trapping (Linsebigler *et al.*, 1995).

In aqueous solution, hydroxyl radicals ($^{\bullet}OH$) production is favorable because of the abundance of hydroxyl groups and water molecules on the surface of catalyst. However, in the gas phase, organic substrates can themselves act as adsorbed traps for the photogenerated holes since in the gas phase, water molecules are not the predominant species in contact with the catalyst. Although in the presence of water vapor, hydroxyl groups are presented on the catalyst surface and their contribution to photooxidation cannot be discarded (Alherici *et al.*, 1997).

When adsorbed water molecules are oxidized by holes, hydroxyl radicals, which have strong oxidizing power, are formed (Equations 3.5 and 3.6).

$$h^{+} + H_2O \rightarrow {}^{\bullet}OH + H^{+} \qquad (3.5)$$

$$h^{+} + OH^{-} \rightarrow {}^{\bullet}OH \qquad (3.6)$$

The hydroxyl radicals can then react with organic components, initially producing free radicals. When molecular oxygen is present (reactions always occur in the presence of oxygen in the air for the use of the photocatalyst for environment), it can react with these free radicals producing organic peroxyl

radicals. These radicals then take part in chain reactions. In a short time, organic compounds are completely degraded, i.e., converted into carbon dioxide and water.

Meanwhile, the electrons that are produced in the electron-hole pairs reduce (i.e., add electrons) oxygen in air. Because oxygen can be reduced more easily than water, it will tend to be reduced, producing the superoxide radical anion (O_2^-) as seen in Equation 3.7

$$e^- + O_2 \rightarrow O_2^- \qquad (3.7)$$

The superoxide anion attaches itself to the peroxyl radicals mentioned above. The resulting unstable product now contains at least four oxygens and can decompose to produce a carbon dioxide molecule. On the molecular scale, superoxide acts like a "supercharge", greatly increasing the oxidation process. In addition to this mechanism, another interpretation proposed recently is that the formation of atomic oxygen ($O^\bullet$), which is extremely reactive in air, leads to a direct attack on the carbon bonds in organic material.

3.2 Sol-gel method (Fu et al., 1996; Su et al., 2004)

The sol-gel process occurs in liquid solution of organometallic precursors such as tetraethyl orthosilicate, zirconium propoxide and titanium isopropoxide, which, by means of hydrolysis and condensation reaction (Equations 3.8 to 3.10), leads to the formation of sol.

$$M\text{-}O\text{-}R + H_2O \Rightarrow M\text{-}OH + R\text{-}OH \quad \text{(hydrolysis)} \qquad (3.8)$$

$$M\text{-}O\text{-}H + HO\text{-}M \Rightarrow M\text{-}O\text{-}M + H_2O \quad \text{(water condensation)} \qquad (3.9)$$

$$M\text{-}O\text{-}R + HO\text{-}M \Rightarrow M\text{-}O\text{-}M + R\text{-}OH \quad \text{(alcohol condensation)} \qquad (3.10)$$

A typical example of a sol-gel method is the addition of metal alkoxides to water. The alkoxides are hydrolyzed giving the oxide as a colloidal product.

The sol is made of solid particles of a diameter of few hundred nanometers suspending in a liquid phase. After that, the particles condense into gel, in which solid macromolecules are immersed in a liquid phase. Drying the gel at low temperature (25-100˚C) produces porous solid matrices or xerogels. To obtain a final product, the gel is heated. This heat treatment serves several purposes, i.e., to remove solvent, to decompose anions such as alkoxides or carbonates to give oxides, to rearrange of the structure of the solid, and to allow crystallization to occur.

Using the sol-gel method, one can easily control a stoichiometry of solid solution and a homogeneous distribution of nanoparticles and metal oxides. In addition, the advantages are that the metal oxides can be prepared easily at room temperature and high purity can be obtained.

3.3 Materials employed as photocatalysts

The catalyst used for photocatalytic process is called “photocatalyst”. The photochemical process involves electronic structure of photocatalyst. Photocatalysis starts when the photocatalyst is exposed to the light. After that, light is absorbed by photocatalyst leading to generation of electrons (e^-) and holes (h^+). The semiconductor metal oxides that are usually used in photocatalytic reaction include TiO_2, ZnO, Al_2O_3, SiO_2, ZrO_2, CeO_2, SnO_2, Fe_2O_3, $SrTiO_3$ and $BaTiO_3$.

In this research we focus on the effects of doping of cerium dioxide on properties and photocatalytic activities of doped titanium dioxide prepared by a sol-gel method. This section discusses properties and applications of the two metal oxides, namely, titanium dioxide and cerium dioxide.

3.3.1 Titanium dioxide

3.3.1.1 Physical and Chemical Properties (Othmer, 1991; Fujishima et al., 1999)

Titanium dioxide has three crystal structures: anatase, which tends to be more stable at low temperature; brookite, which is usually found only in minerals and has a orthorhombic crystal structure; and rutile, which is the stable form at higher temperatures. Generally, anatase shows a higher photocatalytic activity than other types of titanium dioxide. Comparison of typical physical properties of rutile, brookite and anatase is displayed in Table 3.1.

Table 3.1 Comparison of properties of rutile, brookite and anatase. (Othmer, 1991 and Fujishima et al., 1999)

Properties	Anatase	Brookite	Rutile
Crystal structure	Tetragonal	Orthorhombic	Tetragonal
Optical	Uniaxial, negative	Biaxial, positive	Uniaxial, negative
Density, g/cm^3	3.84	4.0	4.26
Harness, Mohs scale	$5^1/_2 - 6$	$5^1/_2 - 6$	$7 - 7^1/_2$
Unit cell	$D_4a^{19}.4TiO_2$	$D_2h^{15}.8TiO_2$	$D_4h^{12}.3TiO_2$
Dimension, nm			
a	0.3758	0.9166	0.4584
b	-	0.5436	-
c	0.9514	0.5135	2.953
Refractive index	2.490	-	2.903
Permittivity	31	-	114
Melting point	changes to rutile at high temp	-	1858˚C

The reason that anatase is more photoactive than rutile may lie in the differences in their band structures. The band gap energy of a semiconductor corresponds to the minimum energy of light required to make the material electrically conductive. The band gap energy of anatase is 3.2 eV, which corresponds to UV light with wavelength of 388 nanometers, while the band gap energy for the rutile type is 3.0 eV, corresponding to violet light that has a wavelength of 413 nanometers as shown in Figure 3.4.

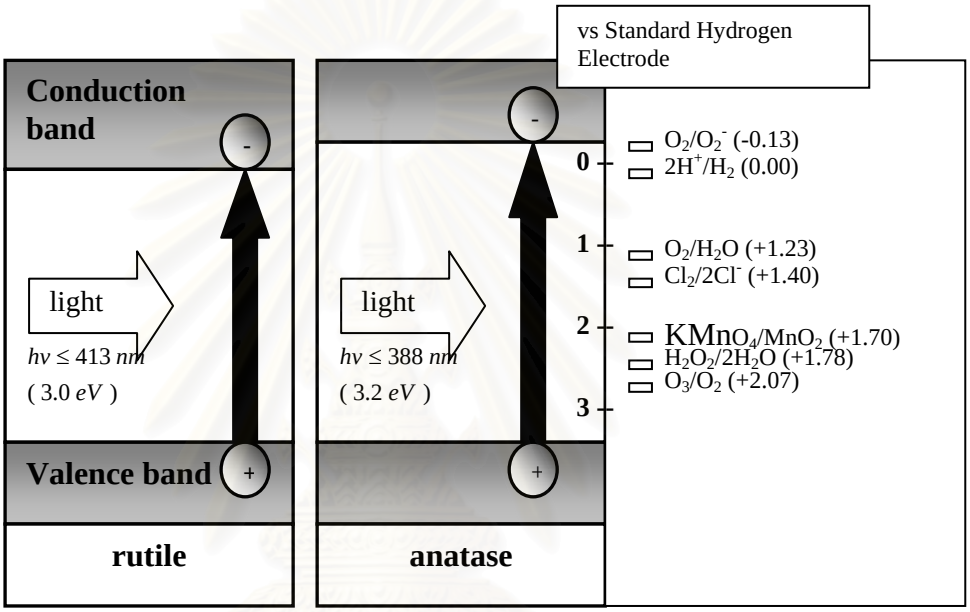

Figure 3.4 Energy diagram for TiO_2 and relevant redox potentials (Fujishima *et al.*, 1999)

The energies of valence band for both anatase and rutile are very low in energy. Consequently, the holes in the valence band (and the hydroxyl radicals) have great oxidizing power. The energy of conduction band for rutile is close to the potential required to electrolytically reduce water to hydrogen gas, but that for anatase is higher in the energy, meaning that it has higher reducing power. Therefore, anatase can drive the very important reaction involving the electrolytic reduction of molecular oxygen (O_2) to superoxide ($O_2^{\bullet -}$).

Although anatase and rutile are both tetragonal, they do not have the same crystal structures. Anatase exists in near-regular octahedral and rutile forms slender prismatic crystal. Rutile is the thermally stable form and is one of the two most important ores of titanium. The crystal structures of anatase and rutile are shown in Figure 3.5.

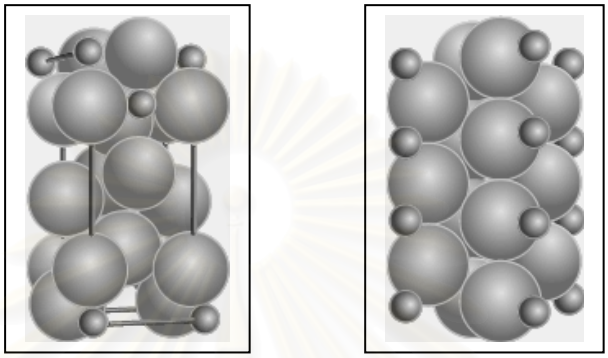

Figure 3.5 crystal structure of anatase (left-hand) and rutile (right-hand) TiO_2

The three forms of titanium (IV) oxide have been prepared in laboratories but only rutile, the thermally stable form, has been obtained in the form of transparent large single crystal. The transformation from anatase to rutile is accompanied by the evolution of ca. 12.6 kJ/mol (3.01 kcal/mol), but the rate of transformation is greatly affected by temperature and by the presence of other substance which may either catalyze or inhibit the reaction. The lowest temperature at which conversion of anatase to rutile takes place at a measurable rate is around 700˚C, but this is not a transition temperature. The change is not reversible since ΔG for the change from anatase to rutile is always negative.

Brookite has been produced by heating amorphous titanium (IV) oxide, which is prepared from an alkyl titanate or sodium titanate, with sodium or potassium hydroxide in an autoclave at 200 to 600 °C for several days. The important commercial forms of titanium (IV) oxide are anatase and rutile and they can readily be distinguished by X-ray diffractrometry.

Since both anatase and rutile are tetragonal structure, they are both anisotropic, and their physical properties, e.g. refractive index, vary according to the direction relative to the crystal axes. In most applications of these substances, the distinction between crystallographic directions is lost because of the random orientation of large numbers of small particles, and only average values of the properties are significant.

Measurement of physical properties, in which the crystallographic directions are taken into account, may be made for both natural and synthetic rutile, natural anatase crystals, and natural brookite crystals. Measurements of the refractive index of titanium (IV) oxide must be made by using a crystal that is suitably orientated with respect to the crystallographic axis as a prism in a spectrometer. Crystals of suitable size of all three modifications occur naturally and have been studied. However, rutile is the only form that can be obtained in large artificial crystals from melts. The refractive index of rutile is 2.903. The dielectric constant of rutile varies with direction in the crystal and with any variation from the stoichiometric formula, TiO_2; an average value for rutile in powder form is 114. The dielectric constant of anatase powder is 48.

Titanium (IV) oxide is thermally stable (mp. 1855 °C) and very resistant to chemical attack. When it is heated strongly under vacuum, there is a slight loss of oxygen corresponding to a change in composition to $TiO_{1.97}$. The product is dark blue but reverts to the original white color when it is heated in air.

3.3.1.2 Applications of titanium dioxide

Titanium dioxide is one of the most common materials in our daily life. Titanium dioxide has been widely used in a variety of paints, plastics, paper, inks, fibers, cosmetics, sunscreens, and foodstuffs.

Naturally, the type of titanium dioxide that is used as a pigment is different from that used as a photocatalyst. The photocatalytic technology is becoming more and more attractive to industries today because environmental pollution has been recognized as a serious problem that needs to be addressed immediately. Various applications in which research and development activities involving titanium dioxide have been investigated, such as anti-fogging activity, anti-bacterial activity, anti-viral activity, fungicidal activity, anti-soiling activity, self-cleaning property and self-sterilizing property, deodorizing effect, photocatalytic air purification, cancer therapy, water treatment and water purification, decomposition of organic compounds as shown in Figure 3.6.

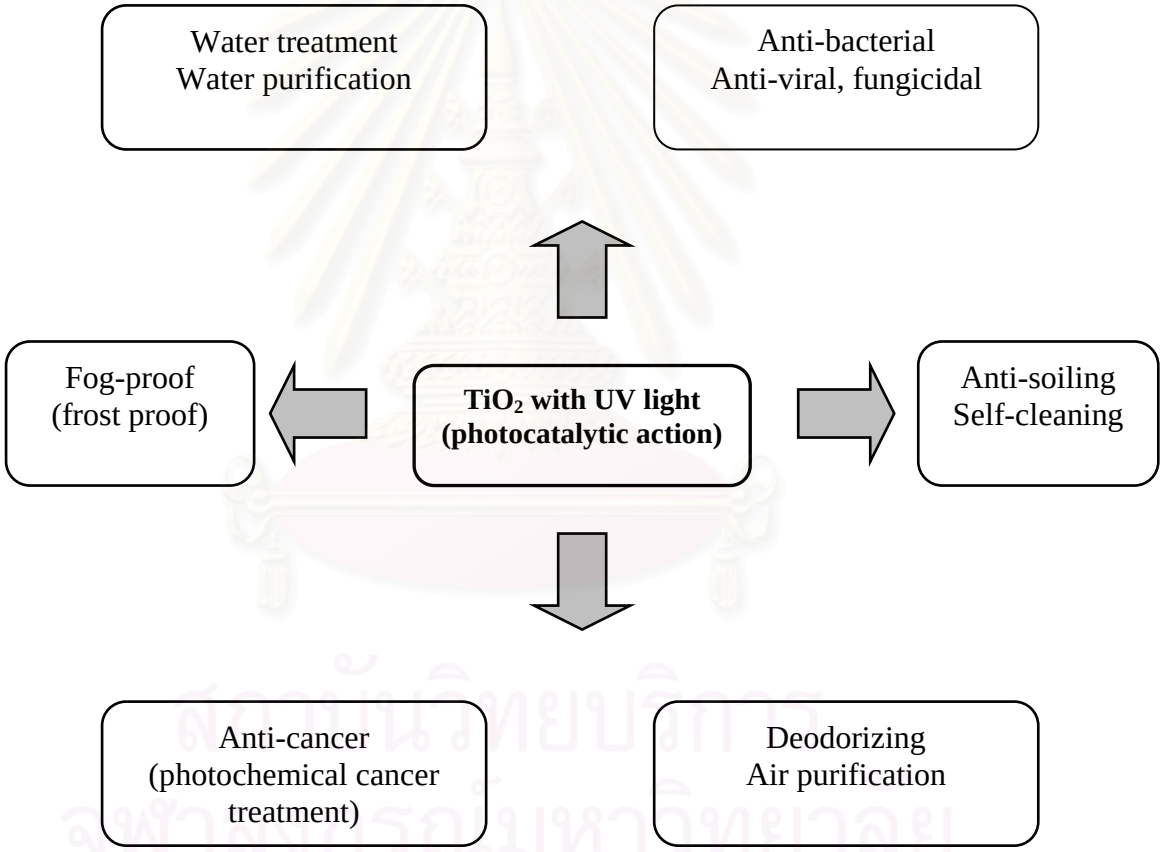

Figure 3.6 application chart of titanium dioxide

Even though a photocatalyst is not suitable for decomposing a large amount of substance in a short time, it can be effective in controlling bacteria and viruses while they are still relatively small in number, before they start multiplying out of control.

3.3.2 Cerium dioxide

3.3.2.1 Physical and Chemical Properties

The band gap energy of cerium dioxide or ceria (CeO_2) with the cerianite or fluorite structure is 2.95 eV, being able to filter out UV rays less than 400 nm in wavelength (Sato *et al.*, 2004). CeO_2 has interesting physicochemical properties. Cerium dioxide is abundant, nontoxic and inexpensive. Furthermore, CeO_2 is a semiconducting material that absorbs light in the near UV and slightly in the visible region. These features make cerium dioxide a promising material that can be used in heterogeneous photocatalytic reactions. Other selected properties of cerium dioxide are given in Table 3.2.

Table 3.2 selected physicochemical properties of cerium dioxide. (Bamwenda et al, 2000)

Properties	Value
Color	Yellowish-white
Density	7.1 g cm^{-3}
Surface area	~9.5 m^2 g^{-1}
Acidity	Weak base
$\Delta H_f{}^o{}_{298}$	-246 kcal mol^{-1}
$T_{melting}$	2873 K
Crystal system	face-centered cubic
Electronegativity	2.3 pauling
Absorption edge	~420 nm
Bandgap[a]	~2.95 eV
Conductivity	1.2-2 x 10^{-8} Ω^{-1} cm^{-1}

[a]The bandgap was estimated from the plot of the UV-VIS absorption vs. wavelength and using the equation : $E_{BG} = 1240/\lambda_{onset}$.

3.3.2.2 Applications of Cerium dioxide

CeO_2 is widely employed as sun screen products and the most used oxygen storing component in automotive three-way catalysts. And ceria is frequently used in combination with other oxides. Cerium dioxide containing materials have been the

subject of numerous investigations in recent years because of their very broad range of applications in catalysis and in advanced ceramic materials. The success of ceria in diverse applications is mainly due to its unique combination of an elevated oxygen transport capacity coupled with the ability to shift easily between reduced and oxidized state ($Ce^{3+} \leftrightarrow Ce^{4+}$). In particular, supported ceria and CeO_2-based mixed oxides are the effective catalysts for the reactions of oxidation of different hydrocarbons and for the removal of total organic carbon from polluted water from different sources. Ceria is used in various catalytic reactions such as CO_2 activation, CO oxidation, CO/NO removal. Despite its widespread applications, the use of pure cerium dioxide is highly discouraged because it is poorly thermostable as it undergoes sintering at high temperature, thereby losing its crucial oxygen storage and release characteristics. Nowadays, CeO_2 can be used as a material for photocatalyst in the photooxidation of water and other VOCs (Bamwenda and Arakawa, 2000).

CHAPTER IV

EXPERIMENTAL

This chapter discusses various materials and methods employed in this research. The chapter is divided into three parts including catalyst preparation, catalyst characterization and photocatalytic activity tests.

Section 4.1 describes preparation of CeO_2/TiO_2 mixed oxides to be used as photocatalysts. Section 4.2 discusses several characterization techniques for catalysts, including X-ray diffractometry, nitrogen adsorption, electron spin resonance spectroscopy, fourier transform infrared spectroscopy, UV-Visible absorption Spectroscopy, inductively coupled plasma atomic emission spectroscopy and X-ray photoelectron spectroscopy. Finally, the experimental apparatus and procedures used in evaluating the performance of the photocatalysts are explained in Section 4.3.

4.1 Catalyst preparation

This section describes methods for preparation of CeO_2/TiO_2 mixed oxides to be employed as photocatalysts using sol-gel processes. All chemicals were of analytical grade and used without further purification. Distilled water was used in all our experiments.

4.1.1 Preparation of TiO_2 and CeO_2-doped TiO_2 nanoparticles

TiO_2 and CeO_2/TiO_2 mixed oxide nanoparticles were prepared via sol-gel method. Titanium (IV) isopropoxide (Aldrich, 97%) and cerium (III) nitrate hexahydrate (Aldrich, 99.99%) were employed as precursors. A solution consisting of 100 ml of titanium isopropoxide and 500 ml of isopropyl alcohol (Aldrich) was added dropwise (5 ml min^{-1}) into 900 ml of distilled water or into $Ce(NO_3)_3$ solution at pH 1.5 (adjusted with nitric acid), while being stirred at room temperature. The suspensions were stirred continuously for approximately 3 days until clear sol was obtained. And then, the sol was dialyzed in a cellulose membrane with a molecular

weight cutoff of 3500 (Spectrum Companies, Gardena, CA). Prior to use, the dialysis tubing was washed in an aqueous solution of 0.001M EDTA and 2% sodium hydrogen carbonate. The washing solution was prepared by dissolving 0.372 grams of EDTA (Asia Pacific Specialty Chemicals Limited) and 43 grams of sodium hydrogen carbonate powder, 99.93% (Fisher Scientific Chemical) in one liter of distilled water. Dialysis tubing was cut into sections of 32 cm in length and was submerged in the washing solution. Then the membrane was heated to 80 °C and held there for 30 minutes while simultaneously being stirred. After the solution was cooled to room temperature, the tubing was again washed with distilled water. The tubing was again immersed in one liter of fresh distilled water while being stirred continuously, and was heated to 80 °C. The tubing was rinsed one more time and was stored in distilled water at 4 °C until needed. The clear sol was placed in dialysis tubing. Then the tubing containing the sol was submerged in distilled water using an approximate ratio of 100 ml of sol per 700 ml of distilled water. The water was changed daily for 3-4 days until the pH of the water reached 3.5. To remove solvents, the dialyzed sol was left in ambient atmosphere overnight and was dried at 110 °C. The resulting gel was then ground. Finally, titania and ceria/titania mixed oxide nanoparticles were calcined to remove impurities at 300 °C for the duration of 2 hours. In this research, CeO_2/TiO_2 mixed oxides were prepared at cerium contents of 0.1%, 0.5%, 1%, 2%, 5% and 10% by mole with respect to titanium. The preparation procedure is shown schematically in Figure 4.1.

4.2 Catalyst characterization

In order to determine physical and chemical properties of catalysts, various characterization techniques were employed. Such techniques are discussed in this section.

4.2.1 X-ray diffractometry (XRD)

XRD was performed to determine crystal phase, bulk crystallinity, and crystallite size of metal oxide. It was conducted using a SIEMENS D5000 X-ray diffractometer with Cu K_α radiation (λ = 1.54439 A^o) with Ni filter. The spectra were scanned at a rate of 0.04^o min^{-1} in the 2θ range of 20-80°.

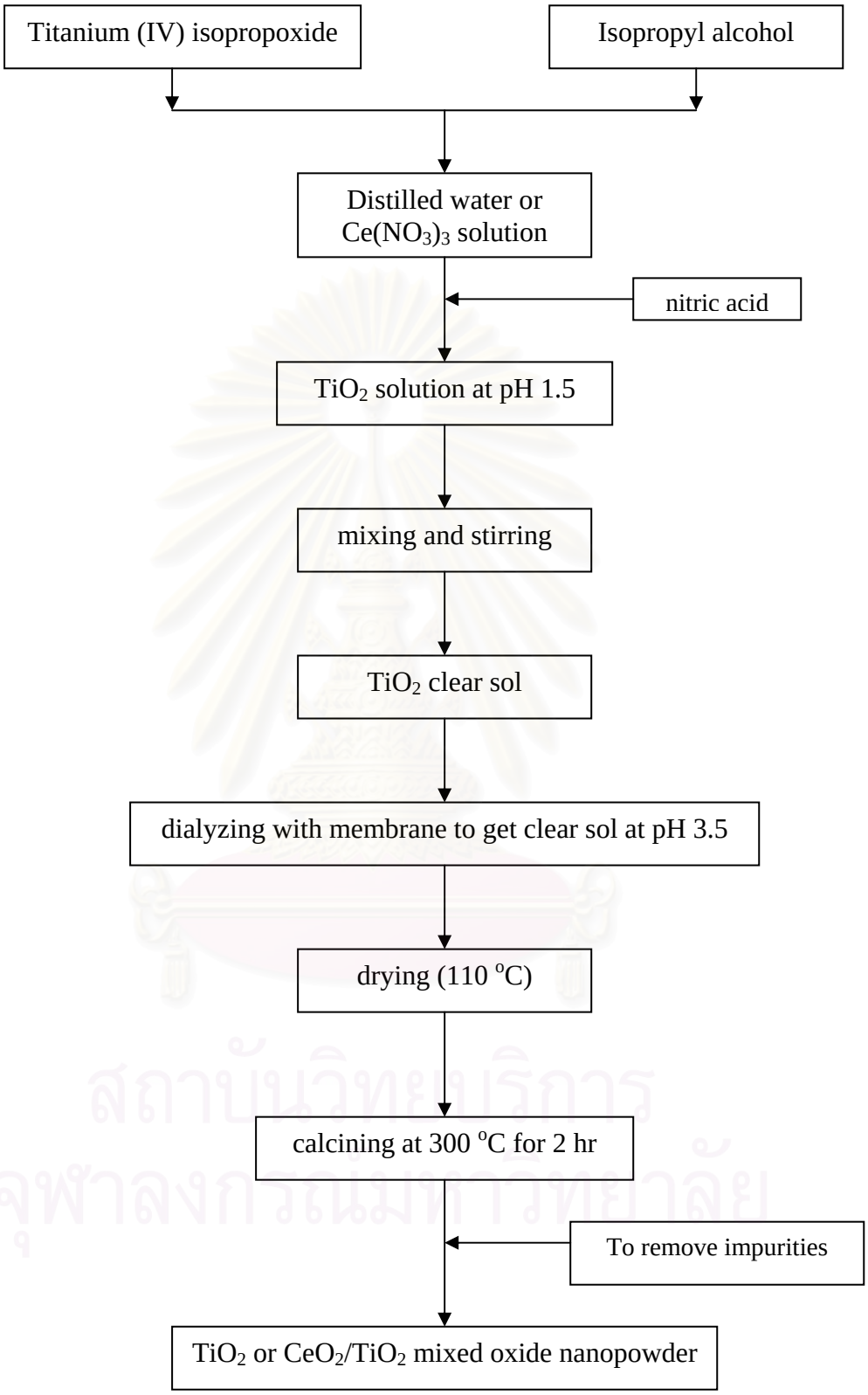

Figure 4.1 Schematic diagram for the preparation method of TiO_2 and CeO_2/TiO_2 samples by sol-gel synthesis

4.2.2 Nitrogen physisorption

The sample's Brunauer-Emmett-Teller (BET) surface area was measured through nitrogen gas adsorption in a continuous flow method at liquid nitrogen temperature. A mixture of nitrogen and helium was employed as the carrier gas using Micromeritics ChemiSorb 2750 Pulse Chemisorption System instrument. The sample was thermally treated at 200 ^{o}C for 1 hr before measurement.

4.2.3 Electron spin resonance spectroscopy (ESR)

ESR measurements were carried out using JEOL JES-RE2X electron spin resonance spectrometer. It was performed to determine the amount of Ti^{3+} surface defect in mixed oxide catalysts. Recorded spectra were scanned and were converted to a g-value scale referring to a Mn^{2+} marker.

4.2.4 Fourier transform infrared spectroscopy (FT-IR)

The functional groups on the catalyst surface were determined using infrared spectroscopy. Before measurement, each sample was mixed with KBr at a ratio of sample to KBr of 1:100 and then was pressed to form a thin wafer. The equipment used was a Nicolet impact 400. IR spectra were recorded from an accumulation of 32 scans in 4000–400 cm^{-1} range with a resolution of 4 cm^{-1}.

4.2.5 Inductively coupled plasma atomic emission spectroscopy (ICP-AES)

Ti and Ce contents in mixed oxide catalysts were determined by inductively coupled plasma (ICP) technique using a optical emission spectrometer (Optima DV2100 Perkin Elmer).

4.2.6 UV-Visible absorption spectroscopy (UV-Vis)

To study the light absorption behavior of the catalysts, the diffuse reflectance spectra (DRS) of the catalyst samples in the wavelength range of 220-800 nm were obtained using a UV-visible scanning spectrophotometer (Perkin Elmer Lambda 650, λ between 220-800 nm and step size 1 nm), while $BaSO_4$ was used as reference.

4.2.7 X-ray photoelectron spectroscopy (XPS)

XPS surface analysis was performed using a Kratos Amicus X-ray photoelectron spectroscopy. The XPS spectra were measured using the following conditions: Mg K_{α} X-ray source at a current of 20 mA and 12 keV; a resolution of 0.1 eV/step; and a pass energy of 75 eV. The operating pressure was approximately 1×10^{-6} Pa. The surface of TiO_2 was cleaned *in situ* using an Ar ion gun sputtering for 30 seconds with 0.5 kV beam voltage and 50 mA emission current. A wide-scan survey spectrum was collected for each sample in order to determine the elements present on the surface. Then, window spectra were recorded for the C 1_s, O 1_s, and the Ti $2p_{3/2}$ and Ti $2p_{1/2}$ photopeaks of each sample. All the binding energies were calibrated internally with the carbon C 1_s photoemission peak at 285.0 eV. Photoemission peak areas were determined after smoothing and background subtraction using a linear routine. Deconvolution of complex spectra were done by fitting with Gaussian (70%)–Lorentzian (30%) shapes using a VISION 2 software equipped with the XPS system.

4.3 Photocatalytic activity tests

The apparatus and experimental procedures employed to evaluate the performance of various photocatalysts were described in this section. The reactants studied in this research to test photocatalytic activity were ethylene (analytical grade, TIG), acetone (analytical grade, Carlo Erba), methanol (analytical grade, Fluka), 2-propanol (analytical grade, Fisher Scientific), and benzene (synthesis grade, Panreac).

4.3.1 Apparatus

Photoreactor system consists of a photoreactor and a gas controlling system.

4.3.1.1 Photoreactor

The photoreactor (see Figure 4.2) had two main components: an ultraviolet light source and the tubular packed bed reactor. The reactor was made from a Pyrex glass tube with a diameter of 5 mm and a length of 27 cm. The stainless steel tube is 1.5″ in length and 3/8″ in diameter connected to the both ends of the

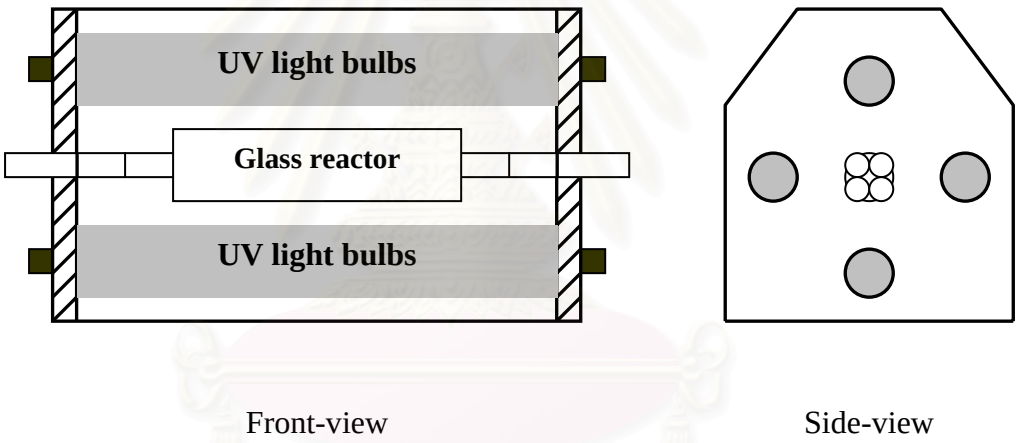

Figure 4.2 Photoreactor set for experiments

reactor. Two sampling points were located on the entrance and exit of the photoreactor. Photocatalyst was packed between two quartz wool layers. The ultraviolet light source was a blacklight blue fluorescent bulbs (8 Watts). Four light bulbs were located 1.5 cm away from the reactor in square configuration. The photoreactor was covered with two layers of aluminum foil to minimize radiation losses from the system.

4.3.1.2 Gas Controlling System

Each feed line reactant was equipped with a mass flow controller and a ball valve. Flow rate of gas was adjusted using a mass flow controller and was measured by a bubble flow meter.

4.3.2 Experimental procedure for determining the activity of the photocatalysts

4.3.2.1 Photocatalytic oxidation of ethylene in gas phase reaction

The photocatalytic activity measurement was performed over 0.2 g of catalyst, which was packed in the reactor. The photoreactor was incorporated into the reactor system. Prior to each experiment, the reactor was supplied with air at a flow rate of 15 ml/min. The photocatalyst was illuminated by ultraviolet light sources for one hour in order to remove any organic compounds that might remain on the surface of the catalyst. After one hour, the reactant, 0.1% (v/v) ethylene in air, was fed to the reactor at a flow rate of 15 ml/min. The temperature of the reactor under illumination was about 90 °C, as measured using a K-type thermocouple. The flow rate of each gas was measured using a bubble flow meter. To investigate the effects of flowrate and humidity on the photocatalytic activities of TiO_2 and CeO_2/TiO_2 catalysts, the flowrate of ethylene at 5 ml min^{-1} and at 15 ml min^{-1} and the humidity of 0% and at 100% were employed in the study. In the case of 100% relative humidity, ethylene feed went through a water saturator. The flow diagram of the apparatus was displayed in Figure 4.3.

The effluent gas was sampled to measure the concentration of ethylene using GC-14B gas chromatrograph (Shimadzu), equipped with a flame ionization detector. The operating conditions for the instrument were listed in Table 4.1. The composition was measured every 20 minutes until steady state was achieved (as indicated by constant peak areas in the gas chromatograms).

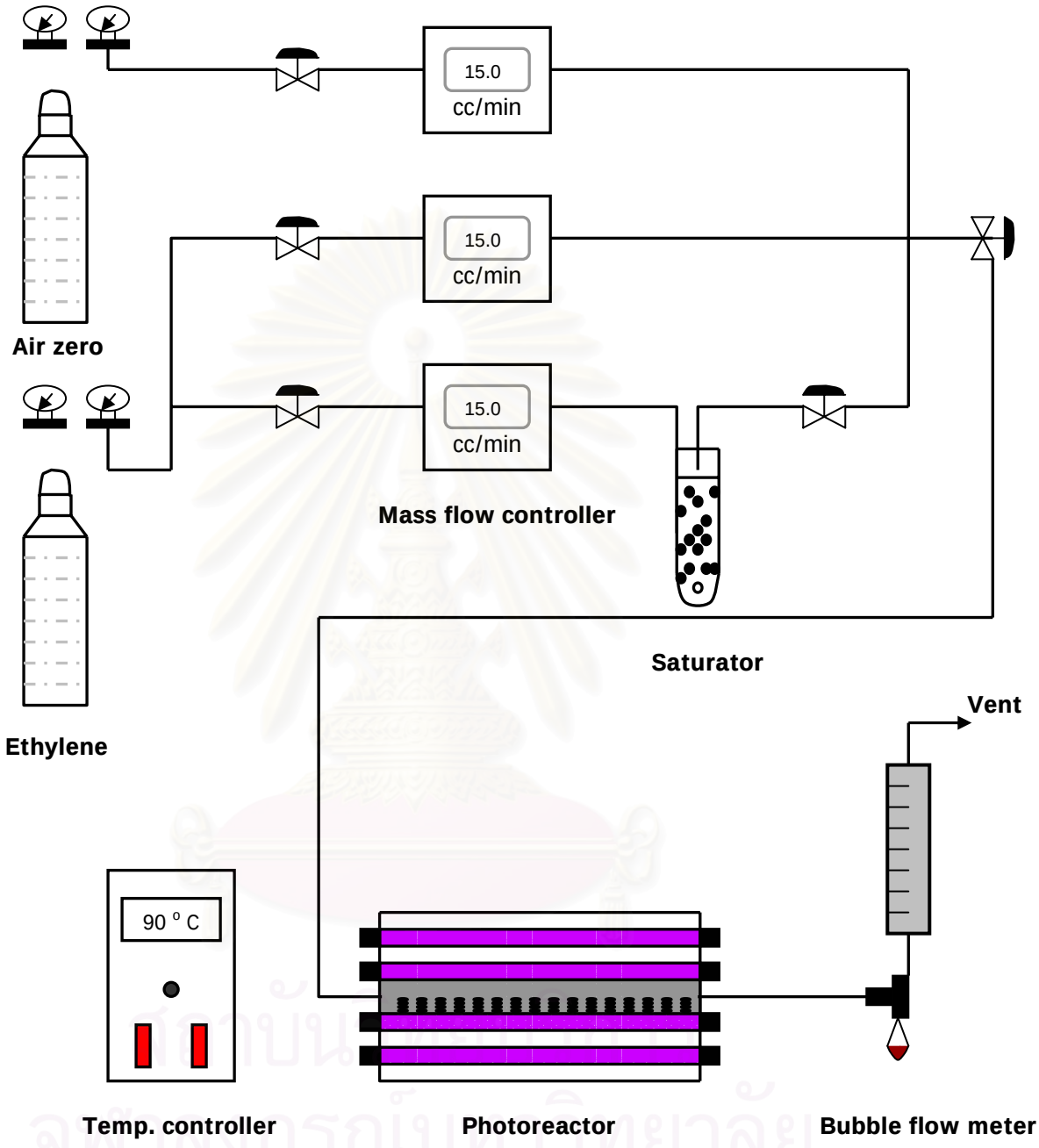

Figure 4.3 Flow diagram of heterogeneous photocatalytic oxidation (PCO)

Table 4.1 Operating conditions for gas chromatography GC-14B

Gas Chromagraph	SHIMADZU GC-14B
Detector	FID
Column	VZ10
Carrier gas	H_2 (99.999%)
Carrier gas flow (ml/min)	30 cc/min
Column temperature	
- initial (^oC)	70
- final (^oC)	70
Injector temperature (^oC)	100
Detector temperature (^oC)	150
Current (mA)	-
Analysed gas	Hydrocarbon C_1-C_4

4.3.2.2 Photocatalytic oxidation of 2-propanol in gas and liquid phases

The photocatalytic activity in the gas phase was performed over 0.2 g of catalyst, which was packed in the reactor. The photoreactor was incorporated into the reactor system. Prior to each experiment, the reactor was supplied with air at a flow rate of 15 ml min^{-1}. The photocatalyst was illuminated by ultraviolet light sources for one hour in order to remove any organic compounds that might remain on the surface of the catalyst. After that, a feed of air zero at a flowrate of 5 ml min^{-1} was bubbled through a saturator that contained aqueous solution of 2-propanol in order to obtain a gaseous mixture of 2-propanol in air. The gaseous mixture was then fed to the photoreactor as reactants. The temperature of the reactor under illumination was about 90 °C, as measured using a K-type thermocouple. The flow rate of the gas was measured using a bubble flow meter.

For the liquid phase reaction, the reactant is an aqueous solution of 2-propanol with a concentration of 5 mol/l. 200 ml of the reactant was placed in a beaker that contained 0.4 g of the catalyst. The ultraviolet light sources, which are two 8W blacklight blue fluorescent lamps, were mounted 10 cm above the beaker. The average light intensities of the lamps are 1.4 mW cm^{-2} for the wavelengths between 300 and 400 nm. Prior to each experiment, the catalyst and the solution were stirred for one hour in order to minimize the effect of adsorption of 2-propanol on the catalyst.

The GC-8A gas chromatrograph (Shimadzu) was used to monitor the changes in the concentration of 2-propanol in both the gas and liquid phases. The operating conditions of GC-8A gas chromatrograph (Shimadzu), equipped with a thermal conductivity detector were listed in Table 4.2. The concentration was measured every 20 minutes until steady state was achieved (as indicated by constant peak areas in the gas chromatograms).

Table 4.2 Operating conditions for gas chromatography GC-8A

Gas Chromagraph	SHIMADZU GC-8A
Detector	TCD
Packed column	Gaskuropack 54
Carrier gas	He (99.98%)
Carrier gas flow (ml/min)	30 cc/min
Length of column	2.5
Mesh size of packing	60/80
Column temperature (^{o}C)	170
Injector temperature (^{o}C)	190
Detector temperature (^{o}C)	190
Current (mA)	80
Analysed gas	Alcohol and light HCs

4.3.2.3 Photocatalytic oxidation of methanol, acetone and benzene in gas phase reaction

The photocatalytic activity in the gas phase was performed over 0.2 g of catalyst, which was packed in the reactor. The photoreactor was incorporated into the reactor system. Prior to each experiment, the reactor was supplied with air at a flow rate of 15 ml min^{-1}. The photocatalyst was illuminated by ultraviolet light sources for one hour in order to remove any organic compounds that might remain on the surface of the catalyst. After that, a feed of air zero at a flowrate of 5 ml min^{-1} was bubbled through a saturator that contained aqueous solution of methanol, acetone or benzene for each experiment in order to obtain a gaseous mixture of chemicals in air. The gaseous mixture was then fed to the photoreactor as reactants. The temperature of the reactor under illumination was about 90 °C, as measured using a K-type thermocouple. The flow rate of the gas was measured using a bubble flow meter (see in Figure 4.3).

For methanol and acetone as reactants, the effluent gas was injected to monitor the changes in the concentration of gaseous mixture using GC-8A gas chromatrograph (Shimadzu), equipped with a thermal conductivity detector. The operating conditions for the instrument were as same as the operating conditions of GC-8A gas chromatrograph (Shimadzu) listed in Table 4.2. The concentration was measured every 20 minutes until steady state was achieved (as indicated by constant peak areas in the gas chromatograms).

In the case of benzene, the GC-9A gas chromatrograph (Shimadzu) was used to monitor the changes in the concentration of benzene in the gas phase. The operating conditions of GC-9A gas chromatrograph (Shimadzu), equipped with a flame ionization detector were listed in Table 4.3. The concentration was measured every 20 minutes until steady state was achieved (as indicated by constant peak areas in the gas chromatograms).

Table 4.3 Operating conditions for gas chromatography GC-9A

Gas Chromagraph	SHIMADZU GC-9A
Detector	FID
Column	GP 10% SP-2100
Carrier gas	N_2 (99.999%)
Carrier gas flow (ml/min)	30 cc/min
Column temperature	
- initial (^oC)	110
- final (^oC)	200
Injector temperature (^oC)	250
Detector temperature (^oC)	250
Programme rate (^oC/min)	10
Analysed gas	Benzene and Phenol

The result of photocatalytic activity test was calculated in the term of:

$$\%\ A\ converted\ (\%\ conversion) = \frac{moles\ of\ A\ reacted}{moles\ of\ A\ in\ feed}\ x\ 100\ \%$$

When A is reactant

CHAPTER V

RESULTS AND DISCUSSION

The results and discussion in this chapter are classified into two major parts. In the first part, several characterization techniques for the catalysts including XRD, BET, ICP-AES, FT-IR, ESR, UV-vis and XPS are described. And the photocatalytic activity measurements for photocatalysts in the photocatalytic oxidation of ethylene, 2-propanol, methanol, acetone and benzene will be discussed in the last section.

5.1 Characterization of the catalysts

5.1.1 Determination of cerium dioxide content

Titanium and cerium contents in the catalysts were determined using inductively coupled plasma atomic emission spectroscopy (ICP-AES). From ICP analysis the Ce:Ti atomic ratios of CeO_2/TiO_2 mixed oxides calcined at 300 ^oC for 2 hr at different Ce/Ti ratios were in agreement with calculated amount of cerium used during preparation of CeO_2/TiO_2 mixed oxides (seen in Table 5.1). Slight discrepancies in Ce:Ti atomic ratios was due to incomplete digestion of solid samples with nitric acid solution and filtration step as observed by ICP-AES analysis of the filtrate.

5.1.2 Measurement of specific surface area

The BET surface areas of TiO_2 and CeO_2/TiO_2 catalysts that were calcined at 300 ^oC for 2 hr were determined by nitrogen physisorption and were summarized in Table 5.1. The samples possessed reasonably high specific surface areas in the range of 95-115 m^2 g^{-1}. The CeO_2/TiO_2 mixed oxide with 0.5 mol% Ce possessed the highest surface area of 115 m^2 g^{-1}. And, the specific surface area of CeO_2/TiO_2 catalyst with 1 mol% was the lowest. Reddy and coworkers (2002)

reported that addition of foreign cations (Si^{4+}, Zr^{4+} and Ce^{4+}) prevented the loss of specific surface area at high temperature.

Table 5.1: specific surface areas and Ce:Ti mole ratios of various CeO_2/TiO_2 mixed oxides calcined at 300 ^oC for two hours

Oxide samples	specific surface area ($m^2 g^{-1}$)	Ce:Ti (mol ratio)	
		Calculated value	Measured value
Pure TiO_2	105	-	-
0.1% CeO_2/TiO_2	109	0.001:1	0.001:1
0.5% CeO_2/TiO_2	115	0.005:1	0.004:1
1% CeO_2/TiO_2	95	0.010:1	0.007:1
2% CeO_2/TiO_2	97	0.020:1	0.018:1
5% CeO_2/TiO_2	107	0.050:1	0.044:1
10% CeO_2/TiO_2	103	0.111:1	0.106:1

5.1.3 Crystal structure

The XRD peaks at 2θ = 25.2°, 37.9°, 47.8° and 53.8°, which represent the indices of (101), (004), (200) and (105) planes respectively, of TiO_2 were easily identified as the dominant anatase form, whereas the XRD peaks at 2θ = 27.42° (110) and 54.5° belonged to the rutile form.

The XRD patterns of TiO_2 and CeO_2/TiO_2 samples calcined at 300 ^oC for 2 hr were displayed in Figure 5.1. The major phase of all samples was anatase. The relative intensity of the main anatase peak (101) at 2θ = 25.2° decreased with the increase of cerium content. This decrease might indicate that the doping of cerium ion inhibited the phase transformation of TiO_2 from amorphous into anatase structure.

Additionally, no cerium oxide peaks were observed in the XRD patterns because of a low cerium dosage and incorporation of cerium into TiO_2 lattice.

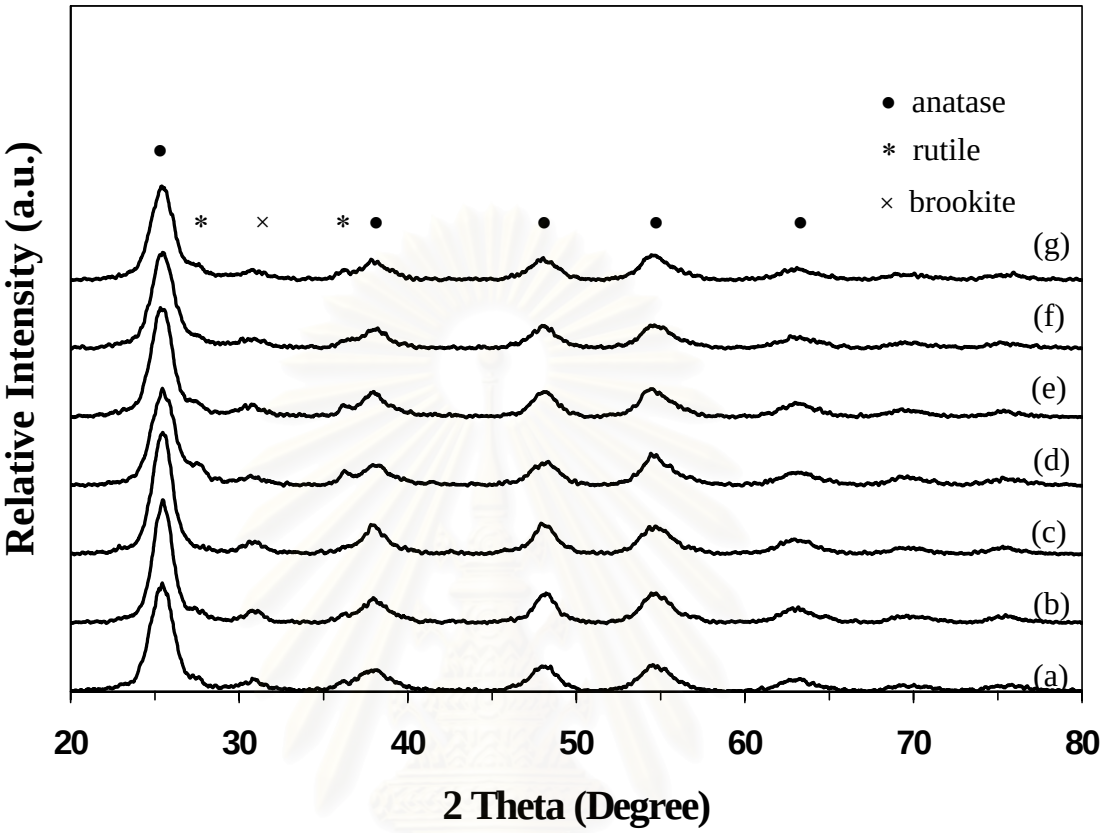

Figure 5.1 XRD patterns of CeO_2/TiO_2 mixed oxides calcined at 300 ^oC for 2 hr; (a) pure TiO_2, (b) 0.1 mol%, (c) 0.5 mol%, (d) 1 mol%, (e) 2 mol%, (f) 5 mol%, (g) 10 mol% CeO_2/TiO_2 catalysts.

The weak peak at $2\theta = 30.86°$ for CeO_2/TiO_2 powder calcined at 300 ^oC for 2 hr was assigned to brookite phase of TiO_2 (see Figure 5.1). Moreover, there was little formation of rutile phase in every sample. Preuss and Gruehn (1994) reported the formation of various Ce-Ti-O oxides, namely, Ce_2TiO_5, $Ce_2Ti_2O_7$ and $Ce_4Ti_9O_{24}$, by heating the appropriate mixtures of solids containing Ce and Ti at 1250 ^oC. However, no such crystalline phase was detected in this case. The absence of crystalline Ce-Ti-O compounds might be due to a different preparation method adopted and lower calcination temperature employed in the present investigation.

The crystallite sizes of anatase titania as calculated from Scherrer Equation were displayed in Table 5.2. The average crystallite size hardly changed when the cerium content increased. The crystallite sizes of either brookite or rutile could not be determined because their observed XRD peaks were too small. The specific surface areas of CeO_2/TiO_2 samples were comparable to that of the pure TiO_2 sample. Both the crystallite sizes and the specific surface areas indicated that the textural and bulk structural properties of the mixed oxide were not significantly altered upon ceria addition.

Table 5.2: Specific surface areas and crystallite sizes of various CeO_2/TiO_2 mixed oxides calcined at 300 ^oC for two hours

Sample	Specific surface area ($m^2 g^{-1}$)	Crystallite size (nm)	Crystal lattice parameter		Crystal volume (A^{o3})
			a cell (A^o)	*c* cell (A^o)	
Pure TiO_2	105	5	3.782	9.368	134.00
0.1% CeO_2/TiO_2	109	6	3.774	9.281	132.19
0.5% CeO_2/TiO_2	115	6	3.800	9.021	130.26
1% CeO_2/TiO_2	95	5	3.768	9.489	134.72
2% CeO_2/TiO_2	97	5	3.776	9.789	139.57
5% CeO_2/TiO_2	107	5	3.788	8.994	129.05
10% CeO_2/TiO_2	103	5	3.792	9.220	132.58

5.1.4 Fourier Transform Infrared Spectroscopy (FT-IR) measurements

The FT-IR spectra of TiO_2 and CeO_2/TiO_2 catalysts are displayed in Figure 5.2. A peak at the wavenumber of 3675 cm^{-1} corresponding to a stretching vibration of Ti-OH group was observed in every sample. At a wavenumber of 1620 cm^{-1}, a band assigned to water was also observed.

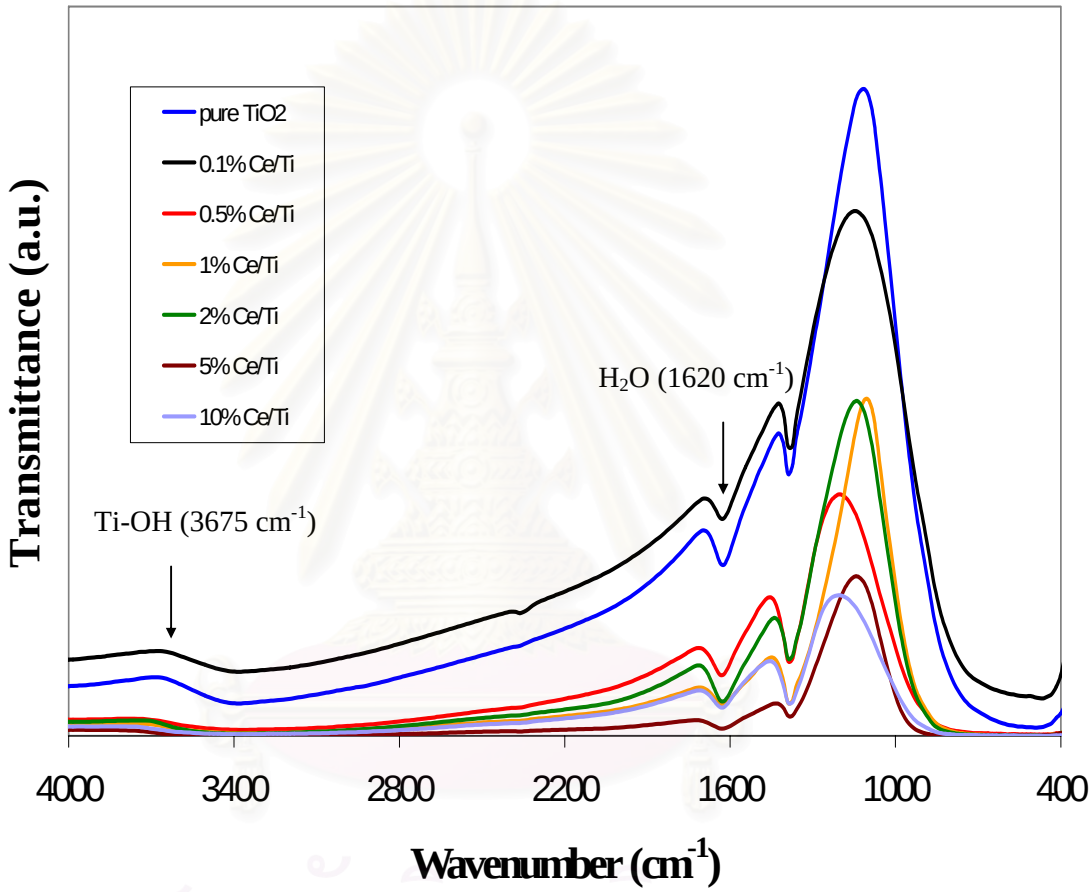

Figure 5.2 FT-IR spectra of various CeO_2/TiO_2 mixed oxides calcined at 300 ^oC for two hours; (a) pure TiO_2, (b) 0.1 mol%, (c) 0.5 mol%, (d) 1 mol%, (e) 2 mol%, (f) 5 mol% and (g) 10 mol% CeO_2/TiO_2 catalysts.

From FT-IR spectra, the bond corresponding to Ti-OH bonds appeared at a wavenumber of 3675 cm^{-1}. The sites on the TiO_2 surface that bonded with OH-groups were Ti^{4+} sites. When cerium content increased, the hydroxyl group on the catalyst surface decreased (as suggested by smaller peak at 3675 cm^{-1}).

5.1.5 UV-Visible Absorption Spectroscopic (UV-Vis) measurement

UV-visible spectra of pure TiO_2 and CeO_2/TiO_2 mixed oxides calcined at 300 ^oC for two hours were shown in Figure 5.3. To investigate the optical absorption properties of catalysts, we examined the diffuse reflectance spectra of TiO_2 and CeO_2/TiO_2 catalysts in the range of 200-800 nm. The results indicated that pure TiO_2 had no absorption in the visible region (> 400 nm), while CeO_2/TiO_2 samples had gradually higher absorption in the region between 400-500 nm as the cerium content increased. The spectra of ceria-titania suggested that incorporation of ceria into TiO_2 induced a small red-shift of the absorption with respect to the pure titania. In addition, the optical absorption of the mixed oxides in the UV region was also enhanced.

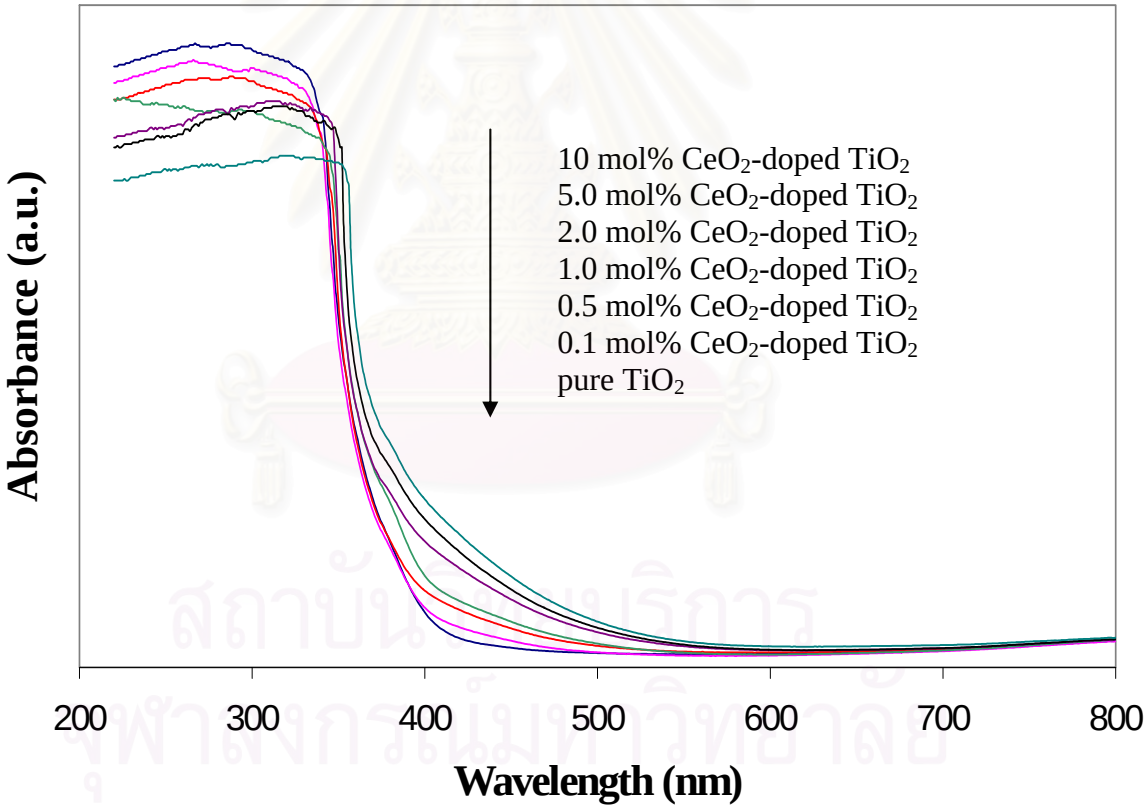

Figure 5.3 The UV-vis diffuse reflectance spectra of TiO_2 and CeO_2/TiO_2 mixed oxide catalysts calcined at 300 ^oC for two hours.

From Figure 5.3, pure TiO_2 had the maximum light absorption in the UV region when compared to CeO_2/TiO_2 mixed oxides. Light absorption by a catalyst resulted in photogeneration of electron-hole pairs, which led to photocatalytic activity

of the catalyst. The optimum concentration of CeO_2/TiO_2 might be associated with the most efficient separation of photogenerated electron-hole pairs. Pleskov (1981) reported that the value of space charge region potential for the efficient separation of electron-hole pairs must be not lower than 0.2 V. As the concentration of CeO_2 phase increased, the impurity band would become broader and, thus, the charge separation gap became narrower. Consequently, the recombination of electron-hole pairs would occur more rapidly.

5.1.6 Electron spin resonance (ESR) measurements

Figure 5.4 displays the results obtained from ESR measurements at 77 K with liquid nitrogen in vacuum for TiO_2 and CeO_2/TiO_2 mixed oxides. The peak observed was assigned to Ti^{3+} surface defects. As cerium content increased, the Ti^{3+} peak became smaller and thus the amount of Ti^{3+} surface defect decreased. The data of the amount of Ti^{3+} surface defect was given in Table 5.3.

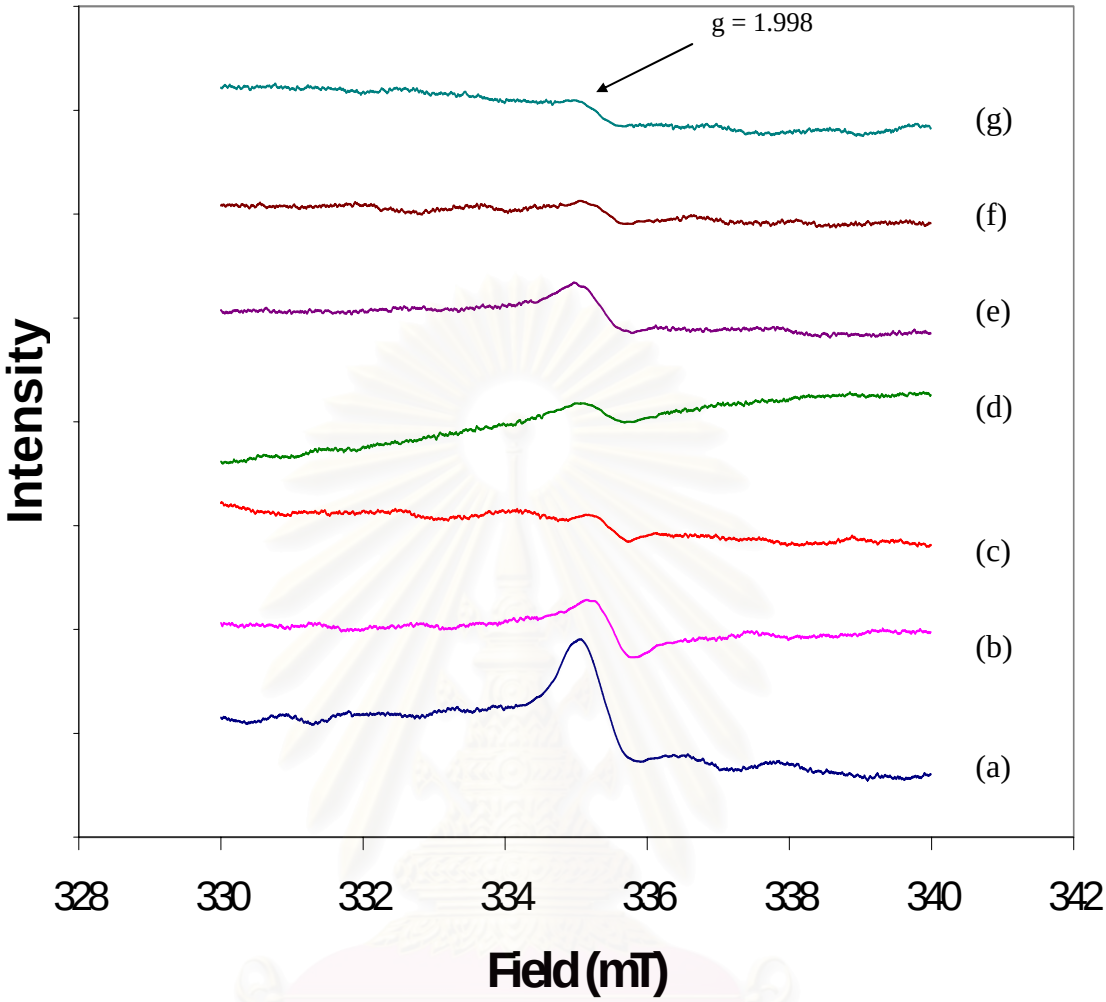

Figure 5.4 ESR spectra of CeO_2/TiO_2 mixed oxides calcined at 300 ^oC for two hours; (a) pure TiO_2, (b) 0.1 mol%, (c) 0.5 mol%, (d) 1 mol%, (e) 2 mol%, (f) 5 mol%, (g) 10 mol% CeO_2/TiO_2 catalysts. The amount of Ti^{3+} surface defect was related to peak height. The g-value of Ti^{3+} defect was at 1.998.

Table 5.3 The amount of Ti^{3+} surface defects of TiO_2 and CeO_2/TiO_2 mixed oxide catalysts calcined at 300 °C for two hours from ESR measurements

Samples	Crystallite size (nm)	Specific surface area ($m^2 g^{-1}$)	Intensity of Ti^{3+} surface defects per area
Pure TiO_2	5	105	37.4
0.1% CeO_2/TiO_2	6	109	14.8
0.5% CeO_2/TiO_2	6	115	7.5
1% CeO_2/TiO_2	5	95	19.2
2% CeO_2/TiO_2	5	97	8.2
5% CeO_2/TiO_2	5	107	6.9
10% CeO_2/TiO_2	5	103	6.3

5.1.7 X-ray Photoelectron spectroscopic (XPS) measurements

Ti^{3+} surface defects and hydroxyl groups on the catalyst surface were analyzed using X-ray Photoelectron spectroscopy. A survey scan was performed in order to determine the elements on the catalyst surface. Then element scan was carried out for C 1s, O 1s, Ti 2p, and Ce 3d electrons. Binding energies of each element were internally calibrated with carbon (C 1s). Photoemission peak areas were determined using a linear routine. Deconvolution of complex spectra were done by fitting with Gaussian (70%) – Lorentzian (30%) shapes using a VISION 2 software equipped with the XPS system.

According to XPS investigation, the electron binding energies of the main peaks pertaining to Ti 2p and O 1s were summarized in Table 5.4. These values were in good agreement with the values reported in the literatures. Figure 5.5 showed the high-resolution spectra of the Ti 2p and O 1s electrons for 10 %mole CeO_2/TiO_2 mixed oxide catalysts after calcinations at 300 °C for 2 hours. After resolving XPS

curves. The dominant peak at about 530 eV was characteristic of metal oxides, which was in agreement with O 1s electron binding energy arising from ceria and titania lattice. The oxygen atoms in the titania matrix were the primary contribution to the spectrum. Another O 1s peak at 532 eV was attributed to surface hydroxyl groups.

Table 5.4 XPS binding energy values for TiO_2 and various CeO_2/TiO_2 samples after calcinations at 300 ^oC for two hours.

Samples	**Binding energy (eV)**			
	Ti 2p		**O 1s**	
	Ti $2p_{1/2}$	**Ti $2p_{3/2}$**	**OH^-**	**$O_{lattice}$**
Pure TiO_2	459.1	464.8	531.5	530.4
0.1% CeO_2/TiO_2	458.9	464.6	531.8	530.2
0.5% CeO_2/TiO_2	458.9	464.6	531.8	530.7
1% CeO_2/TiO_2	459.3	464.8	532.1	531.4
2% CeO_2/TiO_2	459.1	464.8	532.1	531.7
5% CeO_2/TiO_2	459.7	465.1	532.7	531.7
10% CeO_2/TiO_2	459.5	465.2	532.7	531.8

In the Ti 2p XPS spectra of TiO_2 and CeO_2/TiO_2 catalysts, the spin-orbit components ($2p_{3/2}$ and $2p_{1/2}$) of the peak were well deconvoluted by two curves (at approximately 459.2 and 464.8 eV, respectively). These curves indicated that the Ti element mainly existed as the chemical state of Ti^{4+}. As seen in Table 5.4, the doping of ceria almost had no effect on the peak position of Ti 2p. In the case of Ce 3d photoelectron spectra, no peaks of Ce 3d were detected in any samples. The absence of any peaks may be due to too little ceria present in the samples and low calcination temperature. After etching the catalysts under vacuum, the amount of Ti^{3+} defects and hydroxyl groups on the surface of CeO_2/TiO_2 catalysts decreased considerably with the increase of cerium content from 0 to 10% mole (see Table 5.5).

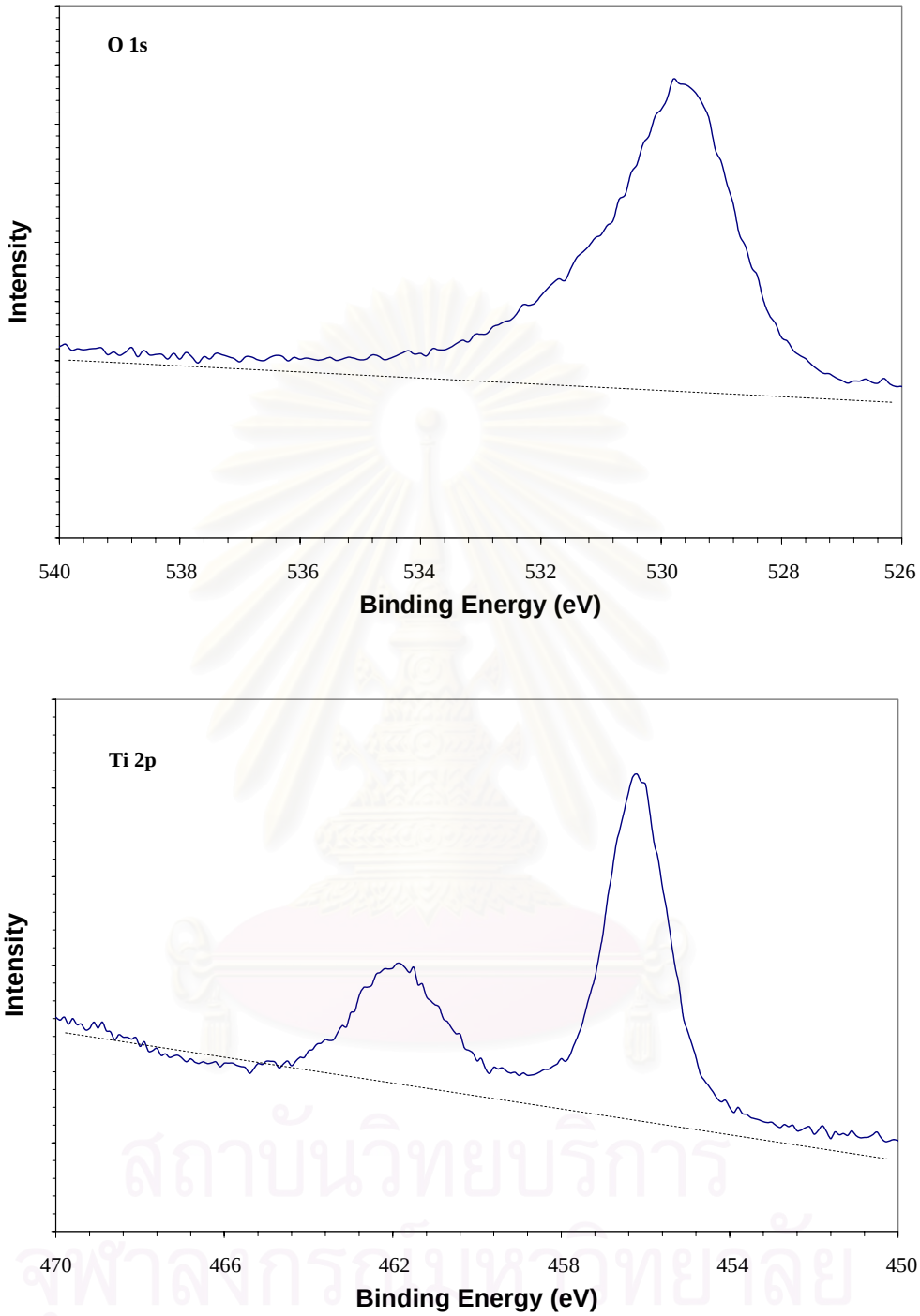

Figure 5.5 Typical XPS O 1s and Ti 2p spectra for 10% mole CeO_2/TiO_2 sample calcined at 300 ^{o}C for two hours

Table 5.5 XPS core-level binding energies (eV) and XPS peak areas for TiO_2 and CeO_2/TiO_2 catalysts calcined at 300 ^oC for two hours after etching.

Catalysts	Area (%)			
	Ti 2p 3/2		O 1s	
	Ti^{3+}	Ti^{4+}	OH^-	O lattice
TiO_2	47.9	52.1	26.1	73.9
0.1%CeO_2/TiO_2	35.6	64.4	20.6	79.4
0.5%CeO_2/TiO_2	24.4	75.6	20.4	79.6
1%CeO_2/TiO_2	29.4	70.5	19.2	80.8
2%CeO_2/TiO_2	19.2	80.8	17.4	82.6
5%CeO_2/TiO_2	16.4	83.6	15.2	84.8
10%CeO_2/TiO_2	15.8	84.2	13.7	86.3

FWHM: Full width at a half of the maximum height of peaks; **BE**: binding energy

5.2 Photocatalytic activity measurements for the catalysts

In this work, TiO_2 and various CeO_2/TiO_2 catalysts synthesized via a sol-gel method were used to test photocatalytic activity in the photocatalytic oxidation of several organic compounds.

5.2.1 Effect of cerium loading in CeO_2/TiO_2 mixed oxides on the photocatalytic oxidation of ethylene

TiO_2 and CeO_2/TiO_2 catalysts with various cerium loading, namely, 0.1%, 0.5%, 1%, 2%, 5%, and 10% mol, were employed in the measurements of the photocatalytic activities in the ethylene photodegradation. The photocatalytic reaction was operated at 90 ^oC and a flowrate of 15 ml min^{-1} of 0.01% vol ethylene in air under UV illumination. The main products occurred in this reaction were carbon dioxide and water.

Figure 5.6 shows conversion of ethylene as a function of cerium loading in CeO_2/TiO_2 mixed oxide photocatalysts. The photocatalytic activity dramatically decreases with an increase of cerium loading. The maximum conversion of 35.0% belonged to pure TiO_2 while 10% CeO_2/TiO_2 catalyst gave the minimum conversion at 3.3%. Addition of cerium to the catalyst lowered the amount of Ti^{3+} on the catalyst surface of TiO_2, which was confirmed by ESR results (see Figure 5.4). Ti^{3+} surface defects could act as traps to promote the charge transfer. These defects on the TiO_2 surface could suppress the recombination of electron-hole pairs and hence extend their lifetime to participate in the reaction. So the higher content of Ti^{3+} on the catalyst surface would improve the interfacial charge transfer and enhance the photocatalytic activity.

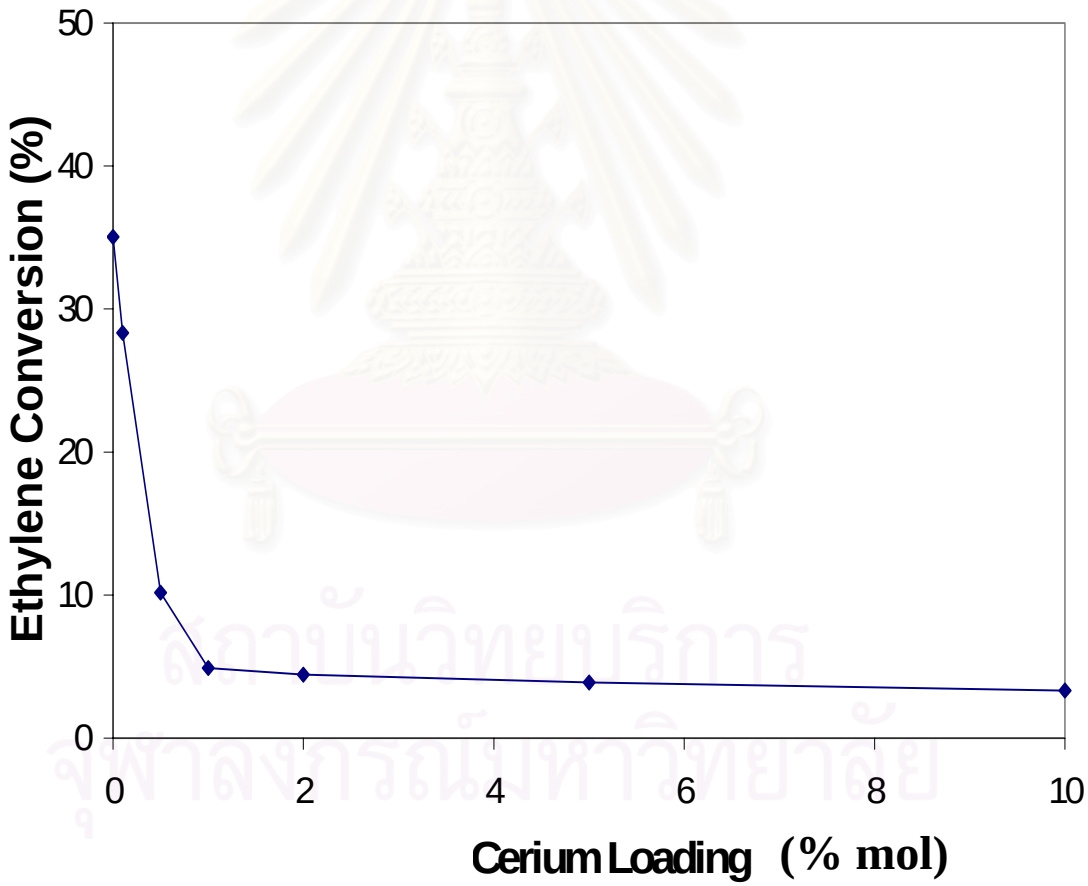

Figure 5.6 Influence of cerium content on the activities of CeO_2/TiO_2 mixed oxides for photocatalytic oxidation of ethylene. The flowrate of 0.01% vol. ethylene in air was 15 ml min^{-1} and 0.2 g of photocatalyst was used.

From UV-Visible spectroscopic results (see section 5.1.5), pure TiO_2 had no light absorption in the visible region while CeO_2/TiO_2 catalysts absorbed more visible light with increasing cerium content. In contrary, in the UV region pure TiO_2 had the highest light absorption when compared to CeO_2/TiO_2 catalysts. And light absorption performance would decrease when cerium content of mixed oxides increased. Therefore, the decrease in the photocatalytic activities of CeO_2/TiO_2 catalysts might be as a result of the lower light absorption in the UV-range. More light absorption would increase the electron-hole activation and brought about enhancement of the photocatalytic activities. Additionally, the smaller band-gap energy of the catalysts with the increase in cerium content resulted in the lower separation of photogenerated of electron-hole pairs. Consequently, the recombination of electron-hole pairs would occur more rapidly. This phenomenon would lower the photocatalytic activities of CeO_2/TiO_2 mixed oxides.

Another effect of addition of ceria was the hydroxyl group content on the catalyst surface. From FT-IR and XPS analyse, number of hydroxyl groups on the catalyst surface decreased with an increase in cerium content. Lin and Yu (1998) reported that the lower photocatalytic activity for CeO_2/TiO_2 mixed oxide was attributed to larger isoelectric point of the mixed oxide. High isoelectric point led to fewer hydroxide ions on the surface of catalyst. Hydroxide ion acted as traps for holes to prevent recombination of electrons and holes. Surface hydroxyl group played a major role on the photocatalytic reaction. In addition to acting as hole traps, surface hydroxyl groups could also be oxidized by holes to produce hydroxyl radicals, which were powerful oxidants. More hydroxyl groups on the catalyst surface would decrease the recombination of electron-hole pairs and enhanced the photocatalytic activity of catalyst. From the experiment, pure TiO_2 that had the most hydroxyl groups on the catalyst surface would give the best photocatalytic activity.

5.2.2 Effect of flowrate on the activities of CeO_2/TiO_2 mixed oxides in photocatalytic oxidation of ethylene

The effect of flowrate of ethylene on photocatalytic oxidation of ethylene could be seen in Figure 5.7. Photocatalytic activities of pure TiO_2 were the highest at conversions of 63.1% and 35.0% for flow rates of 5 ml min^{-1} and 15 ml min^{-1}, respectively. The photocatalytic activities of CeO_2/TiO_2 catalysts decreased as cerium content increased for both flow rates. The reasons for the decrease were discussed in Section 5.2.1.

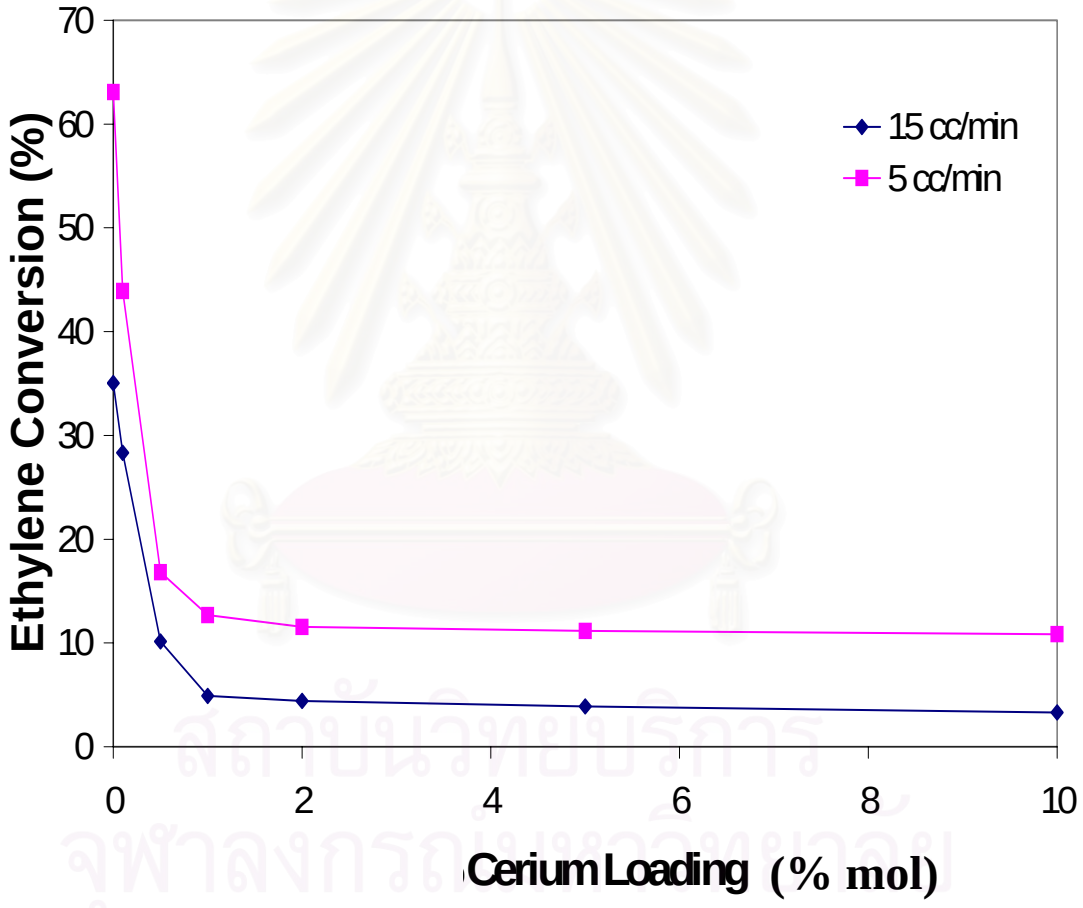

Figure 5.7 Effect of flow rate of reactant on the photocatalytic activities of CeO_2/TiO_2 catalyst for photocatalytic oxidation of ethylene. Reaction time was 180 min and 0.2 g of catalyst was used.

5.2.3 Effect of humidity on the activities of CeO_2/TiO_2 mixed oxides in ethylene photooxidation

Experiments were performed at a flow rate of 15 ml min^{-1} of ethylene in air to test the photocatalytic activities of TiO_2 and CeO_2/TiO_2 mixed oxides at 0% and 100% relative humidity conditions. The experimental results were shown in Figure 5.8. At 100% relative humidity, pure TiO_2 gave the maximum conversion of 14.4% and the conversion decreased with increasing cerium content. The photocatalytic activities of the catalysts at 100% relative humidity were lower than the values at 0% relative humidity. This result may be attributed to competitive absorption between ethylene and water molecules on the catalyst surface.

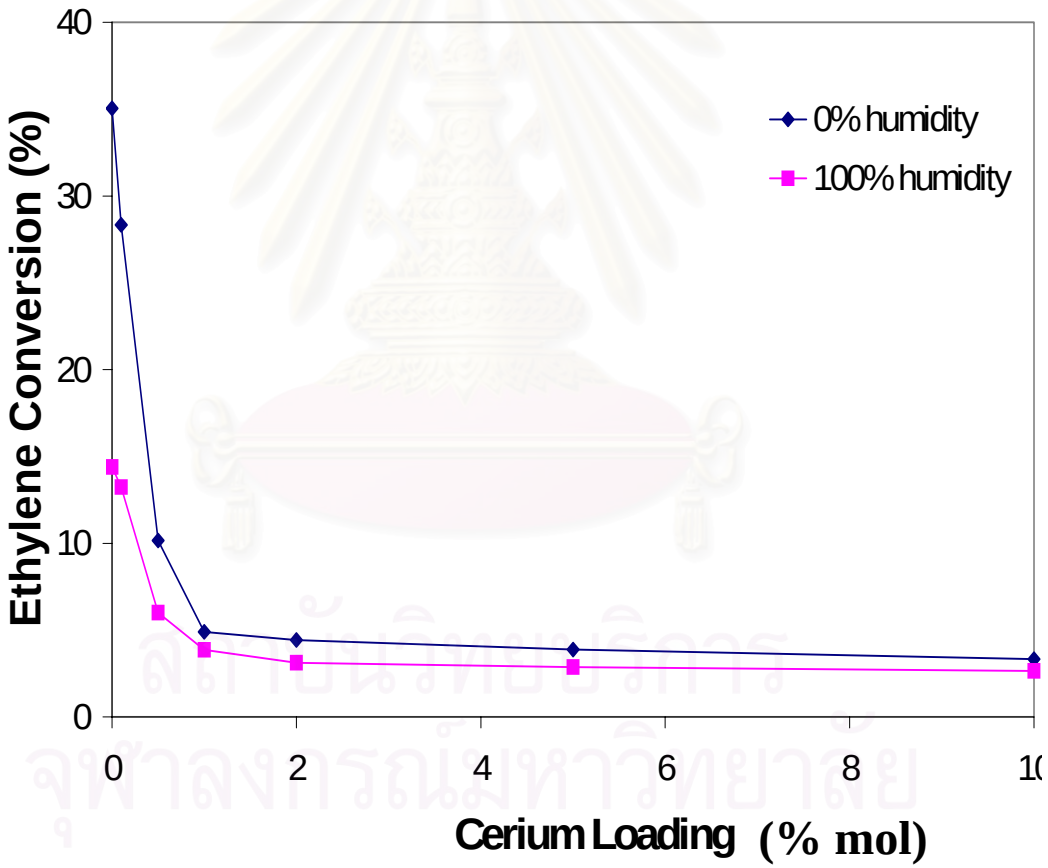

Figure 5.8 Effect of humidity on the activities of CeO_2/TiO_2 mixed oxide for photocatalytic oxidation of ethylene. The reactant gas flowed through 0.2 g of catalyst at a flow rate of 15 ml min^{-1}. Reaction time was 180 minutes.

5.3 Photocatalytic oxidation of other organic compounds over CeO_2/TiO_2 mixed oxides

Four organic compounds, namely, acetone, benzene, methanol, and 2-propanol, underwent photocatalytic oxidation in a tubular photoreactor packed with CeO_2/TiO_2 catalysts. The experimental results could be divided into two groups. Acetone and benzene were in the first group, while methanol and 2-propanol were in the other group.

In the first group, the photocatalytic activities decreased with an increase in cerium content as seen in Figure 5.9. This decrease was in good agreement with the trend observed in photocatalytic oxidation of ethylene previously discussed in Section 5.2. On the other hand, maximum conversions were observed in photocatalytic oxidation of methanol and 2-propanol as cerium content was increased. CeO_2/TiO_2 mixed oxide with 0.5 mol% Ce exhibited the highest activities for the oxidation of both methanol and 2-propanol as shown in Figure 5.10. To explain this difference, one should discuss the reaction mechanism.

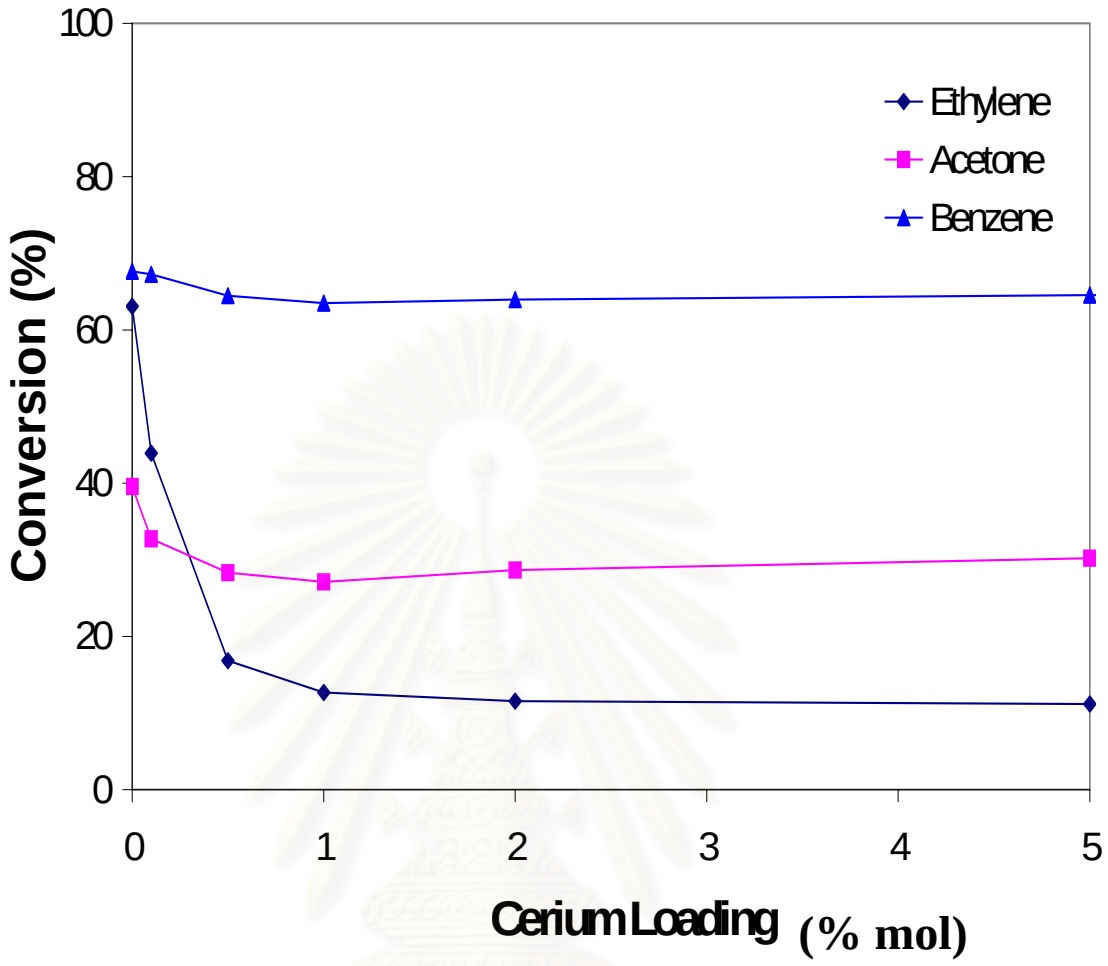

Figure 5.9 Conversion as a function of cerium loading for photocatalytic oxidation of ethylene, acetone and benzene. The reactant gas flowed through 0.2 g of catalyst at a flow rate of 5 ml min^{-1}. Reaction time was 180 minutes.

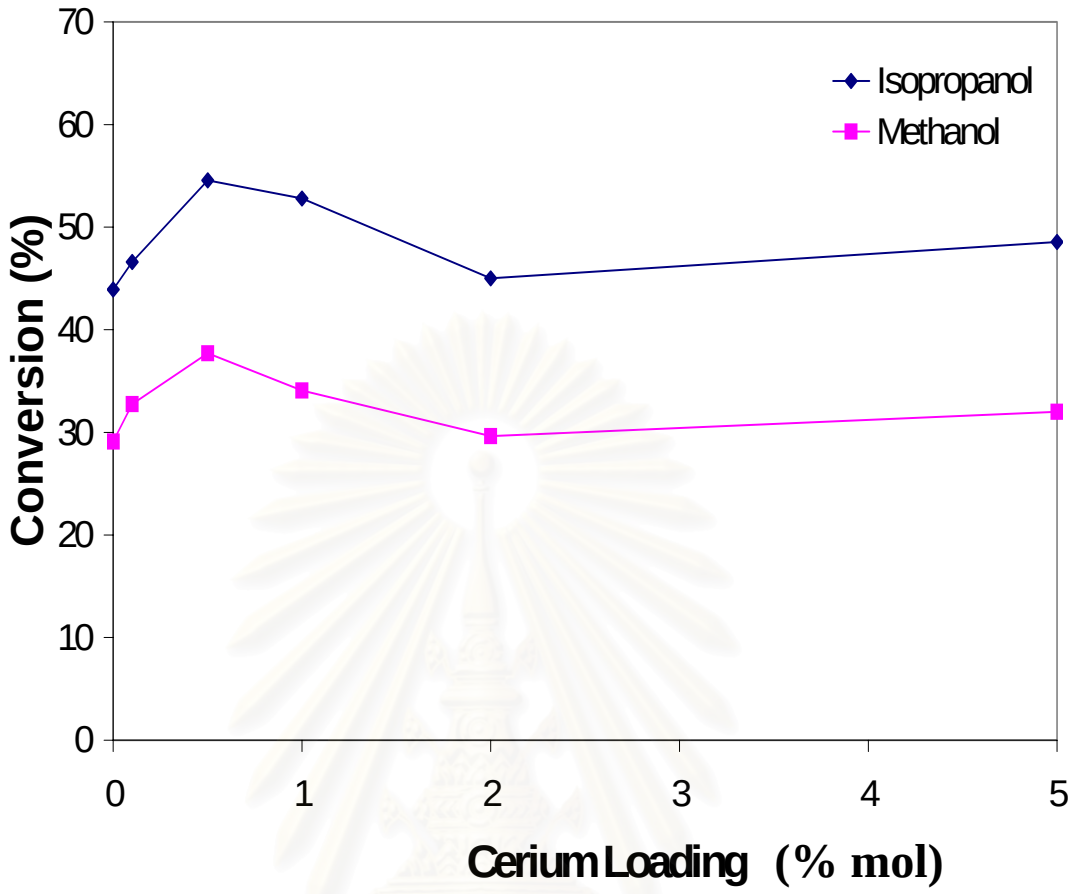

Figure 5.10 Conversion as a function of cerium loading for photocatalytic oxidation of methanol and 2-propanol. The reactant gas flowed through 0.2 g of catalyst at a flow rate of 5 ml min^{-1}. Reaction time was 180 minutes.

Yamazaki and coworkers (1999) proposed a reaction mechanism for photocatalytic oxidation of ethylene. The overall reaction is presented in Equation 5.1 The first steps involved reactant adsorption of reactants on the catalyst surface.

$$C_2H_4 + 3O_2 \Rightarrow 2CO_2 + 2H_2O \quad (5.1)$$

$$C_2H_4 + \sigma \leftrightarrow C_2H_4\sigma \quad (5.2)$$

$$H_2O + \sigma \leftrightarrow H_2O\sigma \quad (5.3)$$

$$O_2 + \sigma' \leftrightarrow O_2\sigma' \quad (5.4)$$

$$TiO_2 + h\upsilon \rightarrow h^+(VB) + e^-(CB) \quad (5.5)$$

$$H_2O\sigma + h^+(VB) \rightarrow OH\sigma + H^+\sigma \quad (5.6)$$

$$OH\sigma + C_2H_4\sigma \leftrightarrow C_2H_4OH\sigma \quad (5.7)$$

$$C_2H_4OH\sigma + O_2\sigma' \rightarrow \text{mineralization to } CO_2 \quad (5.8)$$

σ and σ′ indicated different types of active sites on the TiO_2 surface. Equations 5.2 to 5.4 represented the adsorption-desorption equilibrium for each reactant. The photoexcited electrons were trapped by Ti(IV) centers to form Ti(III). When oxygen is present, the surface Ti(III) was readily oxidized by molecular oxygen to form the superoxide anion.

$$Ti(IV) + e^- \rightarrow Ti(III) \quad (5.9)$$

$$Ti(III) + O_2 \rightarrow Ti(IV) + O_2^- \quad (5.10)$$

Therefore, at the steady state under illumination, oxygen adsorbed exclusively on Ti(III) sites, while water and ethylene adsorbed on Ti(IV) sites. These sites corresponded to σ′ and σ in the reaction scheme, respectively.

The photogenerated electrons were consumed rapidly by reactions denoted in Equations 5.9 and 5.10 under the conditions of excess oxygen concentrations. On the other hand, the holes oxidized the water molecules adsorbed on the catalyst surface to form active hydroxyl radicals (see Equation 5.6).

For CeO_2/TiO_2, the Ce 4f electron played an important role in interfacial charge transfer and suppression of electron-hole recombination. Cerium ions could act as an effective electron scavenger to trap the conduction band electrons of TiO_2. Cerium ions, acting as a Lewis acid, apparently were superior to the oxygen molecule (O_2) in trapping conduction band electrons (Coronado et al., 2002). The electrons trapped at Ce^{4+}/Ce^{3+} sites were subsequently transferred to the surrounding adsorbed O_2. The presence of Ce^{4+} on TiO_2 surface may promote the following processes expressed by Equations 5.11 and 5.12. The formation of $^{\bullet}OH$ may be presented as Equation 5.13 and then a photogenerated electron was transferred

efficiently. For CeO_2/TiO_2 mixed oxide, the formation of labile oxygen vacancies and particularly the relatively high mobility of bulk oxygen species have been reported (Reddy et al., 2003). So ceria had a high oxygen transport and storage capacity (Xie et al., 2003). Hence, the excited electrons might be transferred more easily to O_2 on the surface of CeO_2/TiO_2 catalysts (Li et al., 2005).

$$Ce^{4+} + TiO_2\,(e^-) \rightarrow Ce^{3+} + TiO_2 \quad (5.11)$$

$$Ce^{3+} + O_2 \rightarrow Ce^{4+} + O_2^- \quad (5.12)$$

$$O_2^{\bullet -} + 2H^+ \rightarrow 2\,^{\bullet}OH \quad (5.13)$$

Ammar and coworkers (2001) also proposed the following mechanism for photocatalytic degradation of organic pollutants.

1. Absorption of photons with sufficient energy ($h\nu \geq E_G$ = 3.2 eV) by titania

$$(TiO_2) + h\nu \longrightarrow e^-_{CB} + h^+_{VB} \quad (5.14)$$

2. Neutralization of OH^- groups by photogenerated holes which produces $OH^{\bullet}$ radicals

$$OH^-_{ads} + h^+_{VB} \longrightarrow H^+ + OH^{\bullet} \quad (5.15)$$

3. Oxygen ionosorption (the first step of oxygen reduction, after which oxidation state of oxygen increases from 0 to 1/2)

$$(O_2)ads + e^-_{CB} \longrightarrow O_2^{\bullet -} \quad (5.16)$$

4. Neutralization of $O_2^{\bullet -}$ by protons

$$O_2^{\bullet -} + H^+ \longrightarrow HO_2^{\bullet} \quad (5.17)$$

5. Transient hydrogen peroxide formation

$$2HO_2^{\bullet -} \longrightarrow H_2O_2 + O_2 \qquad (5.18)$$

6. Decomposition of H_2O_2 and second reduction of oxygen

$$H_2O_2 + e^- \longrightarrow OH^\bullet + OH^- \qquad (5.19)$$

7. Oxidation of the organic reactant via successive attacks by $OH^\bullet$ radicals

$$R + OH^\bullet \longrightarrow R'^\bullet + H_2O \qquad (5.20)$$

8. Direct oxidation by reaction with holes

$$R + h^+ \longrightarrow R^{+\bullet} \longrightarrow \text{degradation products} \qquad (5.21)$$

As an example of the last process, holes can react directly with carboxylic acids to generate CO_2

$$RCOO^- + h^+ \longrightarrow R^\bullet + CO_2 \qquad (5.22)$$

From the above reaction scheme, organic compounds could be photodegraded via three reaction pathways. The first pathway was a direct oxidation of reactant with holes (see Equations 5.21 and 5.22). The second pathway was the degradation of organic compounds with hydroxyl radicals obtained from the oxidation of water with holes (see Equations 5.15 and 5.20). And the last pathway was the degradation of organic compounds with hydroxyl radicals obtained from the reduction of oxygen molecules with electrons (see Equations 5.16 and 5.20). Hence, the first two pathways occurred more easily and faster than the last one. Effect of ceria loading to catalysts on photocatalytic performance for each reactant was displayed in Figure 5.9. At a low cerium content, the photocatalytic degradation rate of ethylene dropped more quickly when compared to those of acetone and benzene. It might be due to bond energy of reactant corresponding to the performance of degradation. Ceria had a high oxygen transport and storage capacity (Xie et al., 2003), so it gave rise to the

increasing superoxide anion radicals ($O_2^{\bullet-}$). Photoactivity results were discussed in connection with the characteristics of the radicals observed. EPR measurements confirmed that CeO_2/TiO_2 was photoactivated in the presence of oxygen, giving rise to O_2^- and possibly O_2H radicals. These species might played a role on the photo-oxidation process (Coronado et al., 2002). Among these reactants, ethylene having the lowest bond energy could be degraded easily and quickly; therefore, oxygen molecules trapped by ceria seldom had an effect on the photocatalytic activities. On the other hand, they had an effect on photodegradation of benzene because of its high bond energy compared to bond energies of acetone and ethylene. The activities of CeO_2/TiO_2 catalysts then slightly decreased with an increase of cerium content. The bond energies of organic components as given in table 5.6 were in the following order: benzene > acetone > ethylene.

Table 5.6 Bond energy of ethylene, acetone and benzene

Chemicals	Bond energy (kcal mol^{-1})
Ethylene	~ 537
Acetone	~ 918
Benzene	~ 1263

For the methanol and isopropanol, Ti^{3+} defects on the TiO_2 surface could suppress the recombination of electron-hole pairs and extend their lifetime for the reactions. The mechanism of interfacial charge transfer could be expressed in Equations 5.23 and 5.24 (Szczepankiewicz et al., 2002).

$$Ti^{4+}\text{-O-H} + e^- \rightarrow Ti^{3+}\text{-O-H}^- \quad (5.23)$$

$$Ti^{3+}\text{-O-H}^- + h^+ \rightarrow Ti^{4+}\text{-}^{\bullet}\text{O-H} \quad (5.24)$$

Thus, both Ti^{3+} sites and ceria sites had effects on the photocatalytic activity of catalyst. The roles of both sites in photodegradation were similar, that is, trapping oxygen and electron. From ESR and XPS measurements, the number of Ti^{3+} sites on the CeO_2/TiO_2 surface compared to that of pure TiO_2 decreased with increasing ceria loading. In contrary, the number of cerium sites became larger when

ceria loading increased. This opposing effect should give rise to optimal value of ceria loading, according to Figure 5.11. And the optimal value of ceria loading appeared to be 0.5 mol% in the cases of methanol and 2-propanol.

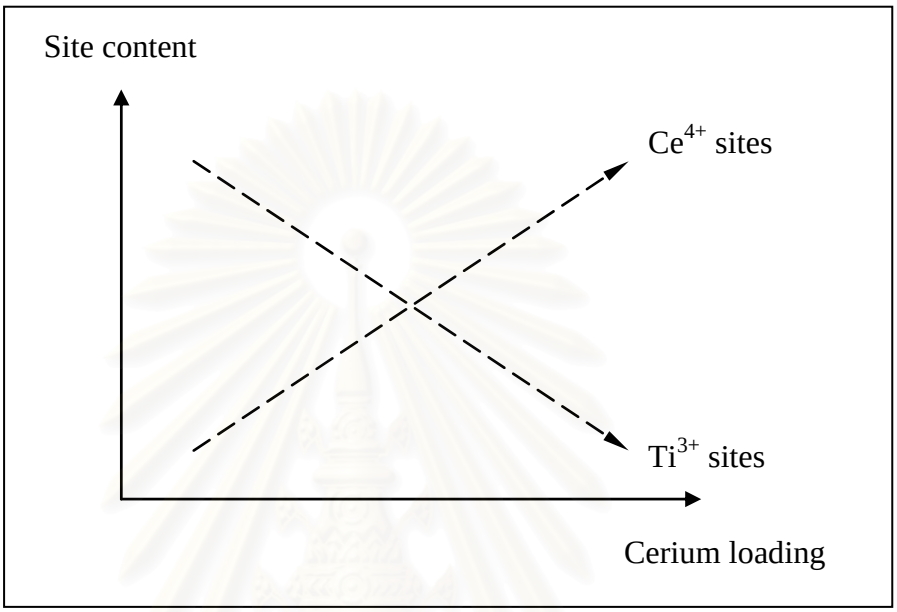

Figure 5.11 Effect of cerium addition on Ti^{3+} surface sites and ceria sites

From the reaction mechanism, organic compounds and water vapor were adsorbed on Ti^{4+} surface sites, while oxygen molecules were adsorbed on Ti^{3+} sites. Then organic compounds were oxidized by holes to form organic radicals that were unstable and easy to react. A small content of cerium added to catalysts would assist in trapping oxygen, resulting in higher activity. When cerium loading exceeded the optimal value, the Ti^{3+} surface sites and also Ti^{4+} sites would abruptly decrease. This caused higher recombination of electron-hole pairs and lower for photo-oxidation of alcohol (methanol and 2-propanol) as seen in Figure 5.10.

Thus, we concluded that the type of reactants has an effect on the photocatalytic activity of CeO_2/TiO_2 catalyst. Photocatalytic oxidation of compound with hydroxyl group was the highest at a low ceria loading.

5.4 Comparison of photocatalytic oxidation of 2-propanol in gas and liquid phases for CeO_2/TiO_2 mixed oxides

Photocatalytic oxidation of 2-propanol was studied in both gas and liquid phases. The experimental results showed that the degradation of 2-propanol in the gas phase had the same trend as the degradation of 2-propanol in the liquid phase, that is, the photocatalytic activities of the catalysts in both phases exhibited maximum values for a cerium loading of 0.5% mol (see Figure 5.12). The major difference between reactions in gas and liquid phases was mass transfer to and from the catalysts. This result suggested that mass transfer process may not be significant in this case and surface reaction was controlling the overall process.

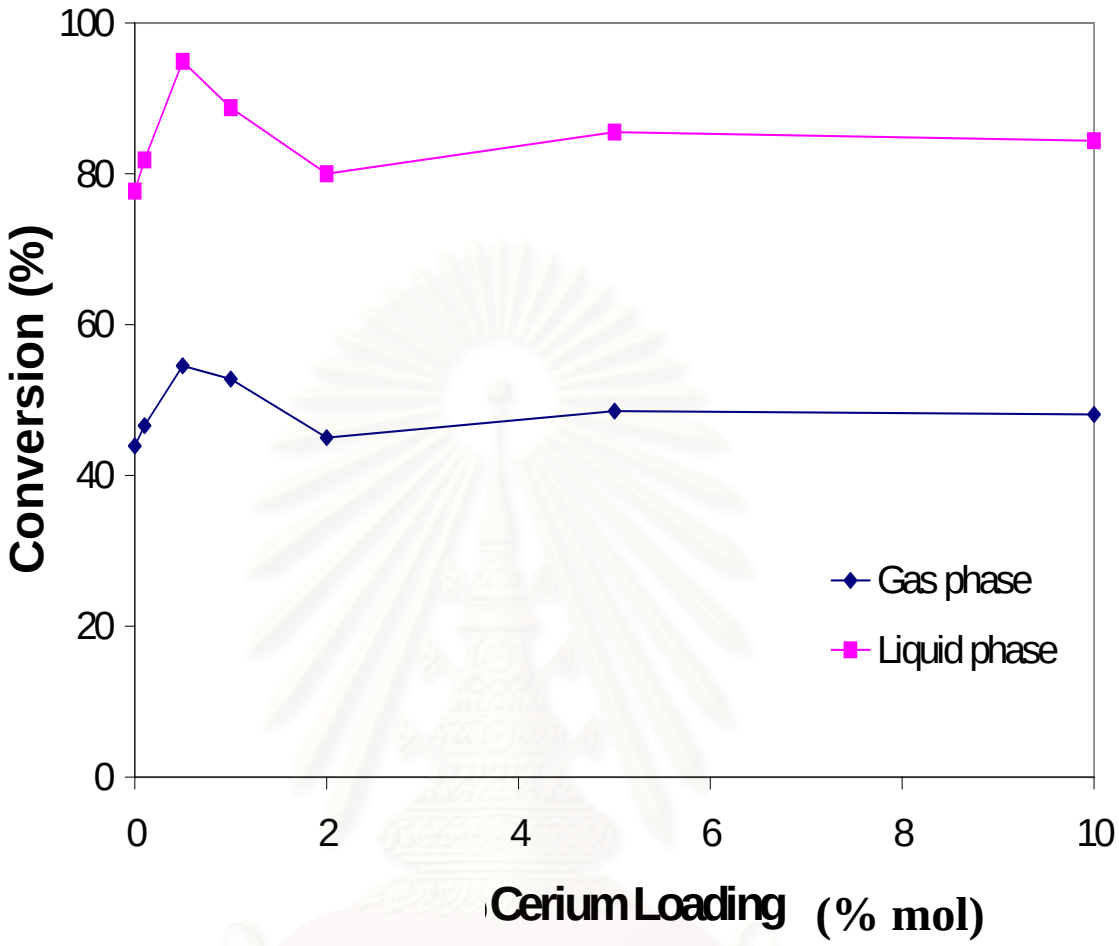

Figure 5.12 Conversion as a function of cerium loading for photocatalytic oxidation of 2-propanol over CeO_2/TiO_2 catalysts in gas and liquid phases. Reaction time was three hours.

CHAPTER VI

CONCLUSIONS AND RECOMMENDATIONS FOR FUTURE RESEARCH

Conclusions and recommendations for future research are presented in this chapter.

6.1 Conclusions

The conclusions of this research are following as:

1. Cerium loading in the range of 0-10% by mole with respect to titanium hardly affected the physical properties of the mixed oxides such as crystal size and phases, and specific surface area.
2. An increase in ceria content in CeO_2/TiO_2 mixed oxides lowered the amounts of Ti^{3+} surface defects and hydroxyl groups on the catalyst surface, reduced the band-gap energy and light absorption in the UV region.
3. An optimal ceria loading of 0.5 mol% was observed with respect to photocatalytic activity of CeO_2/TiO_2 mixed oxides in oxidation of alcohol.
4. Bond energy of chemicals had an effect on the decreasing trend of activity: the decreasing trend of activity for ethylene drastically dropped with a small amount of cerium loading compared to acetone and benzene.

6.2 Recommendations for future studies

From the previous conclusions, the following recommendations for future studies are proposed.

1. Effect of second metal oxide, i.e., in the binary metal oxide should be further investigated in order to understand the actual difference occurred in photocatalytic oxidation.
2. The interaction between CeO_2/TiO_2 and alcohol should also be explored.

REFERENCES

Abdullan, M., Low, G.K.-C., and Matthews, R.W. Effects of common inorganic anions on rates of photocatalytic oxidation of organic carbon over illuminated titanium dioxide, J. Phys. Chem. 94 (1990) 6820-6825.

Alherici, R.M., and Jardim, W.F. Photocatalytic destruction of VOCs in the gas phase using titanium dioxide. Appl. Catal: B 14 (1997) 55-68.

Bamwenda, G.R., and Arakawa, H., Cerium dioxide as a photocatalyst for water decomposition to O_2 in the presence of Ce^{4+} aq and Fe^{3+} aq species, J. Mol. Catal. A 161 (1/2) (2000) 105–113.

Beata Zielin´ska, Antoni Waldemar Morawski, TiO_2 photocatalysts promoted by alkali metals, Appl. Catal. B: Environ. 55 (2005) 221-226.

Chen, H., and Chang, H., Synthesis of nanocrystalline cerium oxide particles by the precipitation method, Ceram. Int. (2005) *In press*.

Chen, P.L., and Chen, I.W., Reactive cerium(IV) oxide powders by the homogeneous precipitation method, J. Am. Ceram. Soc. 76 (6) (1993) 1577–1583.

Dario, M.T., and Bachiorrini, A., Interaction of mullite with some polluting oxides in diesel vehicle filters, Ceram. Int. 25 (6) (1999) 511–516.

De Farias, R., and Airoldi, C., A study about the stabilization of anatase phase at high temperatures on sol–gel cerium and copper doped titania and titania–silica powders, J. Non-crys. Solids 351 (2005) 84-88.

De Nevers, N., Air Pollution Control Engineering, 2nd ed., McGraw-Hill, Singapore, 2000.

DiMonte, R., Fornasiero, P., Graziani, M., and Kasˇpar, J., Oxygen storage and catalytic NO removal promoted by CeO_2-containing mixed oxides, J. Alloys Compd. 277 (1998) 877–885.

Fox, M.A., and Dulay, M.T., Heterogeneous photocatalysis. Chem. Rev. 93 (1993) 341-357.

Fu, X., Clark, L., Zeltner, W., and Anderson , A., Effects of reaction temperature and water vapor content on the heterogeneous photocatalytic oxidation of ethylene. J. Photochem. Photobiol. A: Chem. 97 (1996) 181-186.

Fujishima, A., Hashimoto, K., and Watanabe, T., TiO_2 photocatalysis: fundamental and applications. 1st ed. Tokyo: BKC, 1999.

Gao, L., and Zhang, Q. Effects of amorphous contents and particle size on the photocatalytic properties of TiO_2 nanoparticles, Scripta mater. 44 (2001) 1195-1198.

Garzon, F.H., Mukundan, R., and Brosha, E.L., Solid-state mixed potential gas sensor: theory, experiments and challenges, Solid State Ionics 136/137 (2000) 633-638.

Hester, R.M. Harrison (Eds.), Volatile Organic Compounds in the Atmosphere, The Royal Society of Chemistry, Cambridge, 1995.

Jung, K., and Park, S., and Anpo, M. Photoluminescence and photoactivity of titania particles prepared by the sol-gel technique: effect of calcination temperature, J. Photochem. Photobiol.A: Chem. 170 (2004) 247-252.

Kasˇpar, J., Fornasiero, P., and Hickey, N., Automotive catalytic converters: current status and some perspectives, Catal. Today 77 (4) (2003) 419–449.

Larachi, F., Pierre, J., Adnot, A., and Bernis, A., Ce 3d XPS study of composite $Ce_xMn_{1-x}O_{2-y}$ wet oxidation catalysts, Appl. Surf. Sci. 195 (1–4) (2002) 236–250.

Li, F.B., Li, X.Z., Hou, M.X., Cheah, K.W., and Choy, W.C.H., Enhanced photocatalytic activity of Ce^{3+}–TiO_2 for 2-mercaptobenzothiazole degradation in aqueous suspension for odour control, Appl Catal A: Gen. (2005) *In press*.

Li, Y., White, T., and Lim, S., Structure control and its influence on photoactivity and phase transformation of TiO_2 nano-particles, Rev. Adv. Mater. Sci. 5 (2003) 211-215.

Lin, J., and Yu, J. An investigation on photocatalytic activities of mixed TiO_2-rare earth oxides for the oxidation of acetone in air, J. Photochem. Photobiol. A: Chem. 116 (1998) 63-67.

Linsebigler, A. L., Lu, G. and Yates, Jr. J. T., Photocatalysis on TiO_2 surfaces: principles, mechanism, and selected results. Chem. Rev. 95 (1995) 735-758.

Litter, M.L. Heterogeneous photocatalysis transition metal ions in photocatalytic systems. Appl. Catal. B: Environ. 23 (1999) 89-114.

Liu, Z., Guo, B., Hong, L., and Jiang, H., Preparation and characterization of cerium oxide doped TiO_2 nanoparticles, J. Phys. Chem. Solids 66 (2005) 161-167.

Logothetidis, S., Patsalas, O., and Charitidis, C., Enhanced catalytic activity of nanostructured cerium oxide films, Mater. Sci. Eng. C 23 (6–8) (2003) 803–806.

Maira, A., Yeung, K., Soria, J., Coronado, J., Belver, C., Lee, C., and Augugliaro, V. Gas-phase photo-oxidation of toluene using nanometer-size TiO_2 catalysts, Appl.Catal.B:Environ. 29 (2001) 327-336.

Mohamed, M., Effect of ceria-doped titania on the structure and acidic properties of MoO_3/TiO_2 catalysts, Appl Catal A: Gen. 267 (2004) 135-142.

Nakaoka, M., and Nosaka, Y., ESR investigation into the effects of heat treatment and crystal structure on radicals produced over irradiated TiO_2 powder, J. Photochem. Photobiol. A: Chem. 110 (1997) 299-305.

Othmer, K. Encyclopedia of chemical technology. Vol.6 4th ed. New York: A Wiley-Interscience Publication, John Wiley&Son, 1991.

Park, D., Zhang, J., Ikeue, K., Yamashita, H., and Anpo, M., Photocatalytic oxidation of ethylene to CO_2 and H_2O on ultrafine powdered TiO_2 photocaalysts in the presence of O_2 and H_2O. J. Catal.185 (1999) 114-119.

Reddy, M., and Khan, Stuctural characterization of CeO_2-TiO_2 and V_2O_5/CeO_2-TiO_2 catalysts by Raman and XPS techniques, J. Phys. Chem. B 107 (2003) 5162-5167.

Rynkowski, J., Farbotko, J., Touroude, R., and Hilaire, L., Redox behaviour of ceria–titania mixed oxides, Appl Catal A: Gen. 203 (2000) 335-348.

Sato, T., Katakura, T., Yin, S., Fujimoto, T., and Yabe, S., Synthesis and UV-shielding properties of calcia-doped ceria nanoparticles coated with amorphous silica, Solid State Ionics. 172 (2004) 377–382.

Seethawong, T., Suzuki, Y., and Yoshikawa, S., Synthesis, characterization, and photocatalytic activity for hydrogen evolution of nanocrystalline mesoporous titania prepared by surfactant-assisted templating sol-gel process, J. Solid State chem 178 (2005) 329-338.

Sinha, A.K., and Suzuki, K., Preparation and characterization of novel mesoporous ceria-titania, J. Phys. Chem. B. 109 (2005) 1708-1714.

Sirisuk, A., Hill, C., and Anderson, M. Photocatalytic degradation of ethylene over thin films of titania supported on glass rings, Catal. Today. 54 (1999) 159-164.

Su, C., Hong, B., and Tseng, C., Sol-gel preparation and photocatalysis of titanium dioxide, Catal. Today. 96 (2004) 119-126.

Tashiro, J., Sasaki, A., Akiba, S., Satoh, S., Watanabe, T., Funakubo, H., and Yoshimoto, M., Room-temperature epitaxial growth of indium tin oxide thin films on Si substrates with an epitaxial CeO_2 ultrathin buffer, Thin Solid Films 415 (1/2) (2002) 272–275.

Tsunekawa, S., Fukuda, T., and Kasuya, A., Blue shift in ultraviolet absorption spectra of monodisperse CeO_{2-x} nanoparticles, J. Appl. Phys. 87 (3) (2000) 1318–1321.

Wang, C.H., and Lin, S.S., Preparing an active cerium oxide catalyst for the catalytic incineration of aromatic hydrocarbons, Appl Catal A: Gen. 268 (2004) 227-233.

Wang, S.Z., and Tatsumi, I., Improvement of the performance of fuel cells anodes with Sm^{3+} doped CeO_2, Acta Phys.-Chim. Sin. 19 (9) (2003) 844–848.

Ward, D.A., and Ko, E.I. One-step synthesis and characterization of zirconia-sulfate aerogels as solid superacids, J. Catal. 150 (1994) 18-33.

Wu, N.C., Shi, E.W., Zheng, Y.Q., and Li, W.J., Effect of pH of medium on hydrothermal synthesis of nanocrystalline cerium(IV) oxide powders, J. Am Ceram. Soc. 85 (10) (2002) 2462–2468.

Yamashita, M., Kameyama, K., Yabe, S., Yoshida, S., Fujishiro, Y., Kawai, T., and Sato, T., Synthesis and microstructure of ceria doped ceria as UV filters, J. Mater. Sci. 37 (4) (2002) 683–687.

Yamazaki, S., Fujinaga, N., and Araki, K., Effect of sulfate ions for sol-gel synthesis of titania photocatalyst, Appl. Catal. A: Gen. 210 (2001) 97-102.

Yamazaki, S., Tanaka, S., and Tsukamoto, H., Kinetic studies of oxidation of ethylene over a TiO_2 photocatalyst, J. Photochem. Photobiol A: Chem. 121 (1999) 55-61.

Zhou, X.D., Huebner, W., and Anderson, H.U., Room-temperature homogeneous nucleation synthesis and thermal stability of nanometer single crystal CeO_2, J. Appl. Phys. Lett. 80 (20) (2002) 3814–3816.

APPENDICES

APPENDIX A

CALCULATION OF THE CRYSTALLITE SIZE

Calculation of the crystallite size by Debye-Scherrer equation

The crystallite size was calculated from the width at half-height of the diffraction peak of XRD pattern using the Debye-Scherrer equation.

From Scherrer equation:

$$D = \frac{K\lambda}{\beta \cos \theta} \qquad \text{(A.1)}$$

where D = Crystallite size, Å

K = Crystallite-shape factor = 0.9

λ = X-ray wavelength, 1.5418 Å for CuKα

θ = Observed peak angle, degree

β = X-ray diffraction broadening, radian

The X-ray diffraction broadening (β) is the pure width of a powder diffraction, free of all broadening due to the experimental equipment. Standard α-alumina is used to observe the instrumental broadening since its crystallite size is larger than 2000 Å. The X-ray diffraction broadening (β) can be obtained by using Warren's formula.

From Warren's formula:

$$\beta^2 = B_M^2 - B_S^2 \qquad \text{(A.2)}$$

$$\beta = \sqrt{B_M^2 - B_S^2}$$

Where B_M = The measured peak width in radians at half peak height.

B_S = The corresponding width of a standard material.

Example: Calculation of the crystallite size of titania

The half-height width of 101 diffraction peak = 0.93125^{o}

= 0.01625 radian

The corresponding half-height width of peak of α-alumina = 0.004 radian

The pure width = $\sqrt{B_M^2 - B_S^2}$

= $\sqrt{0.01625^2 - 0.004^2}$

= 0.01577 radian

β = 0.01577radian

2θ = 25.56^{o}

θ = 12.78^{o}

λ = 1.5418 Å

The crystallite size = $\frac{0.9x\,1.5418}{0.01577\ \cos 12.78}$ = 90.15Å

= 9 nm

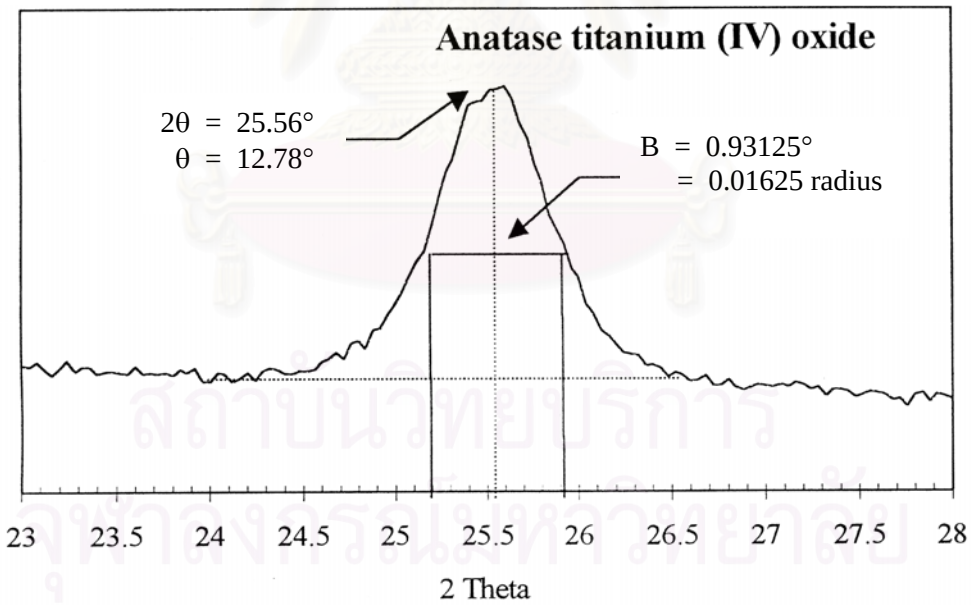

Figure A.1 The 101 diffraction peak of titania for calculation of the crystallite size

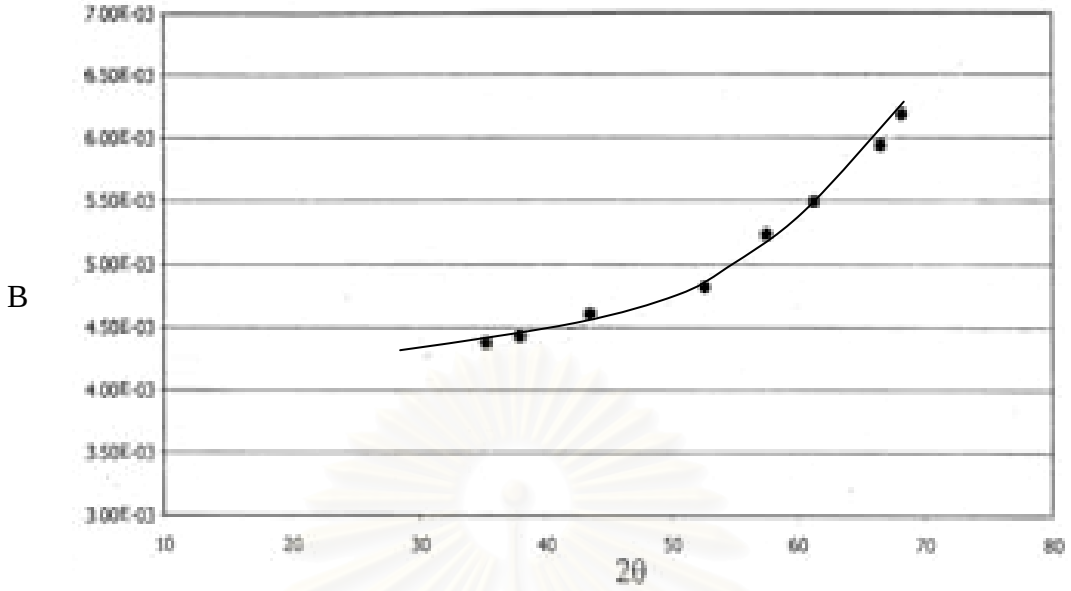

Figure A.2 The plot indicating the value of line broadening due to the equipment. The data were obtained by using α-alumina as standard.

APPENDIX B

THE OPERATING CONDITIONS OF GAS CHROMATOGRAPHY

The composition of hydrocarbons in the product stream was analyzed by a Shimadzu GC14B gas chromatograph equipped with a flame ionization detector. The operating conditions for each instrument are shown in the Table B.1.

Table B.1 The operating condition for gas chromatograph.

Gas Chromagraph	SHIMADZU GC-14B
Detector	FID
Column	VZ10
Carrier gas	H_2 (99.999%)
Carrier gas flow (ml/min)	30 cc/min
Column temperature	
- initial (^oC)	70
- final (^oC)	70
Injector temperature (^oC)	100
Detector temperature (^oC)	150
Current (mA)	-
Analysed gas	Hydrocarbon C_1-C_4

The calibration curve for calculation of composition of ethylene in reactor effluent was obtained and was shown in Figure B.1.

The VZ10 column was used with a gas chromatography equipped with a flame ionization detector to analyze the concentration of products including of ethylene.

Mole of ethylene as y-axis and area determined from gas chromatography as x-axis were plotted. The calibration curve of ethylene was illustrated in the following figure.

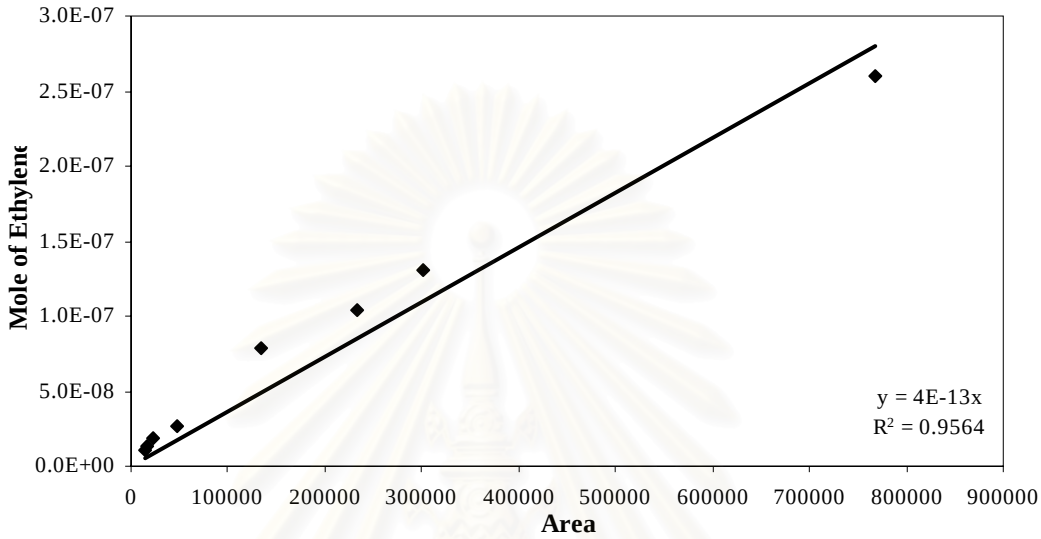

Figure B.1 The calibration curve of ethylene.

APPENDIX C

THE CHARACTERISTIC OF REACTANTS TESTED IN THE PHOTOCATALYTIC OXIDATION

1. Ethylene

Ethylene (or IUPAC name ethene) is the simplest alkene hydrocarbon, consisting of four hydrogen atoms and two carbon atoms connected by a double bond. Because it contains a double bond, ethylene is called an *unsaturated hydrocarbon* or an *olefin*.

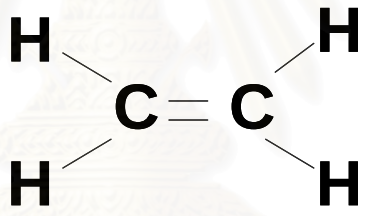

Figure C.1 The structural formula of ethylene

The molecule cannot twist around the double bond, and all six atoms lie in the same plane. The angle made by two carbon-hydrogen bonds in the molecule is 117°, very close to the 120° that would be predicted from ideal sp^2 hybridization.

The double bond is a region of slightly higher electron density, and most of ethylene's chemistry involves other molecules reacting with and adding across its double bond. Ethylene can react with bromine, chlorine, and other halogens, to produce halogenated hydrocarbons. It can also react with water to produce ethanol, but the rate at which this happens is very slow unless a suitable catalyst, such as phosphoric or sulfuric acid, is used. Under high pressure, and, in the presence of a

catalytic metal (platinum, rhodium, nickel), hydrogen will react with ethylene, saturating it.

Table C.1 The specific and thermodynamic properties of ethylene

Properties		Properties	
Systematic name	Ethylene	Boiling point	−103.7 °C
Molecular formula	C_2H_4	Molecular shape	Planar
SMILES	C=C	Dipole moment	Zero
Molar mass	28.05 g/mol	*Thermodynamic* :	
Appearance	Colourless gas	Std enthalpy of	
Phase	Gas	formation ; $\Delta_f H°_{gas}$	+52.47 kJ/mol
Solubility in water	Insoluble	Standard molar	
Flash point	Flammable gas	entropy ; $S°_{gas}$	219.32 $J \cdot K^{-1} \cdot mol^{-1}$
Melting point	−169.1 °C	Bond energy	~ 537 kcal/mol

Except where noted otherwise, data are given for materials in their standard state (at 25°C, 100 kPa)

Applications of ethylene

Ethylene is used primarily as an intermediate in the manufacture of other chemicals, especially plastics. Ethylene may be polymerized directly to produce polyethylene (also called *polyethene* or *polythene*), the world's most widely-used plastic. Ethylene can be chlorinated to produce ethylene dichloride (1,2-Dichloroethane), a precursor to the plastic polyvinyl chloride, or combined with benzene to produce ethylbenzene, which is used in the manufacture of polystyrene, another important plastic. Smaller amounts of ethylene are oxidized to produce chemicals including ethylene oxide, ethanol, and polyvinyl acetate. Ethylene is also a widely-used refrigerant in commercial low temperature systems due to the low boiling point. Ethylene was once used as an inhaled anesthetic, but it has long since been replaced in this role by nonflammable gases. It has also been hypothesized that ethylene was the catalyst for utterances of the oracle at Delphi in ancient Greece

2. Methanol

Methanol, also known as methyl alcohol or wood alcohol, is a chemical compound with chemical formula CH_3OH. It is the simplest alcohol, and is a light, volatile, colorless, flammable, poisonous liquid with a very faint odor. It is used as an antifreeze, solvent, fuel, and as a denaturant for ethyl alcohol.

Methanol is produced naturally in the anaerobic metabolism of many varieties of bacteria. As a result, there is a small fraction of methanol vapor in the atmosphere. Over the course of several days, atmospheric methanol is oxidized by oxygen with the help of sunlight to carbon dioxide and water. Methanol burns in air forming carbon dioxide and water:

$$2\ CH_3OH + 3\ O_2 \rightarrow 2\ CO_2 + 4\ H_2O$$

A methanol flame is almost colorless. Care should be exercised around burning methanol to avoid burning oneself on the almost invisible fire. Because of its poisonous properties, methanol is also used as a denaturant for ethanol. Methanol is often called wood alcohol because it was once produced chiefly as a byproduct of the destructive distillation of wood. It is now produced synthetically by the direct combination of hydrogen and carbon monoxide gases, heated under pressure in the presence of a catalyst.

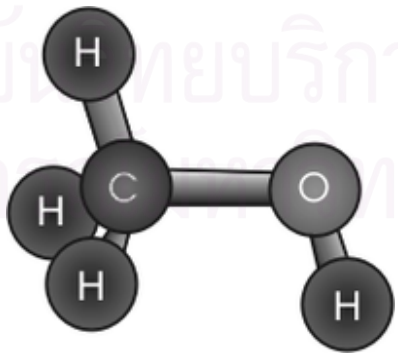

Figure C.2 The structural formula of methanol

Table C.2 The specific and thermodynamic properties of methanol

Properties		Properties	
Systematic name	Methanol	Viscosity	0.59 mPa·s at 20 °C
Molecular formula	CH_3OH	Acidity (pK_a)	~ 15.5
SMILES	CO	Melting point	-97 °C
Molar mass	32.04 g/mol	Boiling point	64.7 °C
Appearance	Colorless liquid	Molecular shape	Tetrahedral and
Phase	Liquid		Bent
Solubility in water	Fully miscible	Dipole moment	1.69 D (gas)
Density	0.7918 g/cm^3	Bond energy	~ 482 kcal/mol

Except where noted otherwise, data are given for materials in their standard state (at 25°C, 100 kPa)

Applications of methanol

Methanol is used on a limited basis to fuel internal combustion engines, mainly by virtue of the fact that it is not nearly as flammable as gasoline. Methanol blends are the fuel of choice in open wheel racing circuits like Champcars, as well as in radio controlled model airplanes, cars and trucks. Dirt circle track racecars such as Sprint cars, Late Models, and Modifieds use methanol to fuel their engines. Drag racers and mud racers also use methanol as their primary fuel source. Methanol is required with a supercharged engine in a Top Alcohol Dragster and all vehicles in the Indianapolis 500 have to run methanol. Mud racers have mixed methanol with gasoline and nitrous oxide to produce more power than gasoline and nitrous oxide alone.

One of the drawbacks of methanol as a fuel is its corrosivity to some metals, including aluminium. Methanol, although only a weak acid, attacks the oxide coating that normally protects the aluminium from corrosion:

$$6CH_3OH + 2Al \rightarrow 2Al^{3+} + 6CH_3O^- + 3H_2$$

The resulting methoxide salts are soluble in methanol, so the corrosion continues until the metal is eaten away.

When produced from wood or other organic materials, the resulting organic methanol (bioalcohol) has been suggested as renewable alternative to petroleum-based hydrocarbons. However, one cannot use BA100 (100% bioalcohol) in modern petroleum cars without modification. Methanol is also used as a solvent and as an antifreeze in pipelines. The largest use of methanol by far, however, is in making other chemicals. About 40% of methanol is converted to formaldehyde, and from there into products as diverse as plastics, plywood, paints, explosives, and permanent press textiles.

In some wastewater treatment plants, a small amount of methanol is added to wastewater to provide a food source of carbon for the denitrification bacteria, which convert nitrates to nitrogen.

In the 1990s, large amounts of methanol were used in the United States to produce the gasoline additive methyl tert-butyl ether (MTBE). The 1990 Clean Air Act required certain major cities to use MTBE in their gasoline to reduce photochemical smog. However, by the late 1990s, it was found that MTBE had leaked out of gasoline storage tanks and into the groundwater in sufficient amounts to affect the taste of municipal drinking water in many areas. Moreover, MTBE was found to be a carcinogen in animal studies. In the resulting backlash, several states banned the use of MTBE, and its future production remains uncertain.

Direct-methanol fuel cells are unique in their low temperature, atmospheric pressure operation, allowing them to be miniaturized to an unprecedented degree. This, combined with the relatively easy and safe storage and handling of methanol may open the possibility of fuel cell-powered consumer electronics.

Other chemical derivatives of methanol include dimethyl ether, which has replaced chlorofluorocarbons as an aerosol spray propellant, and acetic acid.

3. Acetone

In chemistry, acetone (also known as propanone, dimethyl ketone, 2-propanone, propan-2-one and beta-ketopropane) is the simplest representative of the ketones.

Acetone is a colorless mobile flammable liquid with melting point at -95.4 °C and boiling point at 56.53 °C. It has a relative density of 0.819 (at 0 °C). It is readily soluble in water, ethanol, ether, etc., and itself serves as an important solvent. The most familiar household use of acetone is as the active ingredient in nail polish remover. Acetone is also used to make plastic, fibers, drugs, and other chemicals.

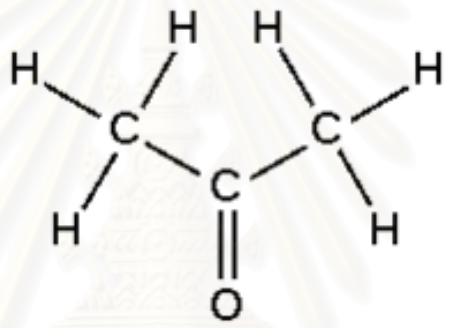

Figure C.3 The structural formula of acetone

Table C.3 The specific and thermodynamic properties of acetone

Properties		**Properties**	
Systematic name	Propanone	Viscosity	0.32 cP at 20 °C
Molecular formula	CH_3COCH_3	Flashpoint	-20 °C
SMILES	CC(=O)C	Melting point	-94.9 °C
Molar mass	58.09 g/mol	Boiling point	56.3 °C
Appearance	Colorless liquid	Molecular shape	trigonal planar at C=O
Phase	Liquid		
Solubility in water	Miscible	Dipole moment	2.91 D
Density	0.79 g/cm^3	Bond energy	~ 918 kcal/mol

Except where noted otherwise, data are given for materials in their standard state (at 25°C, 100 kPa)

Applications of acetone

An important industrial use for acetone involves its reaction with phenol for the manufacture of bisphenol A. Bisphenol A is an important component of many polymers such as polycarbonates, polyurethanes and epoxy resins. Acetone is also used extensively for the safe transporting and storing of acetylene. Vessels containing a porous material are filled with acetone then acetylene, which dissolves into the acetone. One liter of acetone can dissolve around 250 liters of acetylene.

Acetone is often the primary (or only) component in nail polish remover. Acetone is also used as a superglue remover. Small quantities of acetone added to fuel may improve economy and engine performance, though this is only anecdotal and refuted by most automotive engineers.

Acetone has been used in the manufacture of cordite. During World War I a new process of producing acetone through bacterial fermentation was developed by Chaim Weizmann, to help the British war effort.

4. Isopropyl alcohol

Isopropyl alcohol or isopropanol is a common name for propan-2-ol, a colorless, flammable chemical compound with a strong odor. It has the chemical formula $CH_3CHOHCH_3$, and is the simplest example of a *secondary alcohol*, where the alcohol carbon is attached to two other carbons. It is an isomer of propan-1-ol.

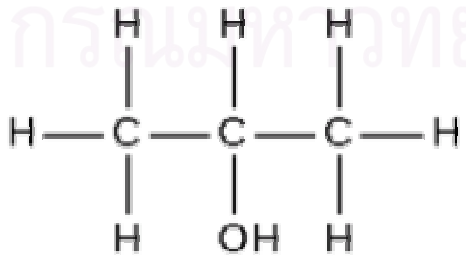

Figure C.4 The structural formula of isopropanol

Table C.4 The specific and thermodynamic properties of isopropanol

Properties		Properties	
Systematic name	Propan-2-ol	Viscosity	1.77 cP at 30 °C
Molecular formula	C_3H_8O	Acidity (pK_a)	16.5 for H on hydroxyl
SMILES	CC(O)C		
Molar mass	60.10 g/mol	Melting point	-88 °C
Appearance	Colorless liquid	Boiling point	82 °C
Phase	Liquid	Flashpoint	12 °C
Solubility in water	Fully miscible	Dipole moment	1.66 D (gas)
Density	0.78 g/cm^3	Bond energy	~ 1034 kcal/mol

Except where noted otherwise, data are given for materials in their standard state (at 25°C, 100 kPa)

Applications of isopropanol

Sterilizing pads typically contain a 60-70% solution of isopropanol in water. Isopropyl alcohol is also commonly used as a cleaner and solvent in industry. It is also used as a gasoline additive for dissolving water or ice in fuel lines. Isopropanol is the main ingredient in rubbing alcohol. It is used as a disinfectant, and is a common solvent.

Isopropanol is a major ingredient in "dry-gas" fuel additive. In significant quantities, water is a problem in fuel tanks as it separates from the gasoline. If the engine tried to combust the water instead of gasoline serious engine problems could result. The isopropanol does not remove the water from the gasoline. Rather, the isopropanol solubilizes the water in the gasoline. Once soluble, the water does not pose the same risk as insoluble water. It is also a very good cleaning agent and often used for cleaning electronic devices such as contact pins (like those on ROM cartridges), magnetic tape deck and floppy disk drive heads, the lenses of lasers in optical disc drives (e.g. CD, DVD) and removing thermal paste from CPUs. It is also used to clean computer monitors, and used by many music shops to give second-hand or worn records a newer looking sheen.

5. Benzene

Benzene, also known as C_6H_6, PhH, and benzol, is an organic chemical compound that is a colorless and flammable liquid with a pleasant, sweet smell. Benzene is a known carcinogen. It is a minor, or additive, component of gasoline. It is an important industrial solvent and precursor in the production of drugs, plastics, gasoline, synthetic rubber, and dyes. Benzene is a natural constituent of crude oil, but it is usually synthesized from other compounds present in petroleum. Benzene is an aromatic hydrocarbon, and the second [*n*]-annulene ([6]-annulene).

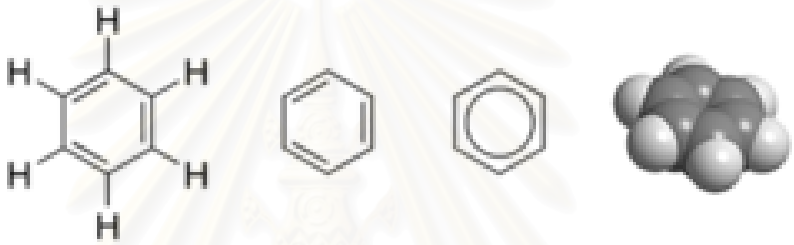

Figure C.5 The structural formula of benzene

Table C.5 The specific and thermodynamic properties of benzene

Properties		Properties	
Systematic name	Benzene	Viscosity	0.652 cP at 20 °C
Molecular formula	C_6H_6	Melting point	5.5 °C
SMILES	C1=CC=CC=C1	Boiling point	80.1 °C
Molar mass	78.11 g/mol	Flashpoint	-11 °C
Appearance	Colorless liquid	Molecular shape	Planar
Phase	Liquid	Dipole moment	0 D
Solubility in water	1.79 g/l (25°C)	Bond energy	~ 1263 kcal/mol
Density	0.8786 g/cm^3		

Except where noted otherwise, data are given for materials in their standard state (at 25°C, 100 kPa)

Applications of benzene

In the 19th and early-20th centuries, benzene was used as an aftershave because of its pleasant smell. Prior to the 1920s, benzene was frequently used as an industrial solvent, especially for degreasing metal. As its toxicity became obvious, other solvents replaced benzene in applications that directly exposed the user to benzene.

Benzene was also used to initially decaffeinate coffee by German importer Lugwig Roselius in 1903. This leads to the production of Sanka, -ka for kaffein, but later discontinued the use of benzene.

As a gasoline additive, benzene increases the octane rating and reduces knocking. As a result, gasoline often contained several the percent of benzene before the 1950s, when tetraethyl lead replaced it as the most widely-used antiknock additive. However, with the global phaseout of leaded gasoline, benzene has made a comeback as a gasoline additive in some nations. In the United States, concern over its negative health effects and the possibility of benzene's entering the groundwater have led to stringent regulation of gasoline's benzene content, with values around 1% typical. European gasoline specifications now contain the same 1% limit on benzene content.

By far the largest use of benzene is as an intermediate to make other chemicals. The most widely-produced derivatives of benzene are styrene, which is used to make polymers and plastics, phenol for resins and adhesives (via cumene), and cyclohexane, which is used in Nylon manufacture. Smaller amounts of benzene are used to make some types of rubbers, lubricants, dyes, detergents, drugs, explosives and pesticides.

In laboratory research, toluene is now often substituted for benzene because of health concerns.

APPENDIX D

CALCULATION OF VAPOR PRESSURE OF SUBSTANCE

Calculation of vapor pressure using Antoine equation

From Antoine equation:

$$\ln P^{sat} = A - \frac{B}{T + C} \qquad (1)$$

where P = vapor pressure of a substance in kPa.

T = temperature in degree Celsius.

A, B, and C = Antoine constants for a given substances.

Example: The vapor pressure of water at 30 ^{o}C is determined as followed;

$$\ln P^{sat} = 16.262 - \frac{3799.89}{30 + 226.35} = 1.4389$$

$$P^{sat} = e^{1.4389} = 4.22\,kPa$$

Table D.1 The vapor pressure of chemicals at 30 ^{o}C by Antoine equation

Chemicals	A	B	C	P^{sat} (kPa)
Acetone	7.11714	1210.595	229.664	11.65
Methanol	8.08097	1582.271	239.726	9.16
Benzene	6.87987	1196.760	219.161	7.98
2-Propanol	8.87829	2010.320	252.636	5.84
Water	16.26200	3799.890	226.350	4.22

APPENDIX E

DETERMINATION OF Ti^{3+} SURFACE DEFECT FROM ESR MEASUREMENT

The amount of Ti^{3+} surface defects from ESR measurement can be relatively determined from:

$$\mathrm{Ti}^{3+}\ \text{surface defects} = \frac{\textit{Intensity of ESR peak height}}{(\textit{surface area})\ x\ (\textit{catalyst weight})} \qquad (1)$$

Example: The Ti^{3+} surface defects of pure TiO_2 are determined as followed;

$$\mathrm{Ti}^{3+}\ \text{surface defects} = \frac{1178.9}{0.3\ x\ 105} = 37.4$$

Table E.1 The relative amount of Ti^{3+} surface defects of TiO_2 and CeO_2/TiO_2 mixed oxide catalysts calcined at 300 °C for two hours

Oxide samples	Catalyst weight (g)	Specific surface area ($m^2\ g^{-1}$)	Intensity of peak height	Intensity of Ti^{3+} surface defects per area
Pure TiO_2	0.3	105	1178.9	37.4
0.1% CeO_2/TiO_2	0.3	109	485.8	14.8
0.5% CeO_2/TiO_2	0.3	115	259.6	7.5
1% CeO_2/TiO_2	0.3	95	550.9	19.2
2% CeO_2/TiO_2	0.3	97	252.5	8.2
5% CeO_2/TiO_2	0.3	107	221.9	6.9
10% CeO_2/TiO_2	0.3	103	183.7	6.3

APPENDIX F

DETERMINATION OF LATTICE PARAMETERS OF TITANIUM DIOXIDE

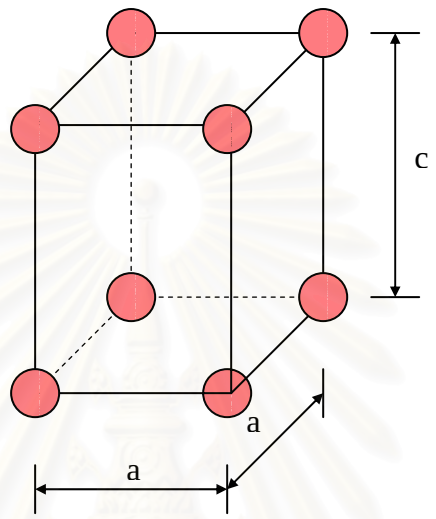

Figure F.1 Tetragonal crystal structure of titanium dioxide

Interplanar spacing (d-spacing) can be calculated from:

$$2d_{hkl}\sin\theta = n\lambda \qquad \text{(Bragg's law)} \qquad (1)$$

So, at a fixed wavelength (controlled by the XRD machine: target, filter, etc.) for a certain value of d (characteristic of samples). After obtaining the d-spacing of each plane, a-cell and c-cell of lattice parameter can be calculated from:

$$d_{hkl} = \frac{a}{[h^2 + k^2 + l^2(\frac{a^2}{c^2})]^{1/2}} \qquad \text{for tetragonal system} \qquad (2)$$

For example, we choose (101) plane and (200) plane of TiO_2 to determine the d-spacing value of each plane

Table F.1 The 2θ value of (101) plane and (200) plane of TiO_2 in each sample from XRD measurement

Oxide samples	2-theta	
	(101) plane	(200) plane
Pure TiO_2	25.44^o	48.20^o
0.1% CeO_2/TiO_2	25.52^o	48.32^o
0.5% CeO_2/TiO_2	25.48^o	47.96^o
1% CeO_2/TiO_2	25.48^o	48.40^o
2% CeO_2/TiO_2	25.32^o	48.28^o
5% CeO_2/TiO_2	25.56^o	48.12^o
10% CeO_2/TiO_2	25.44^o	48.08^o

Determination of d-spacing and lattice parameters for pure TiO_2

From Bragg's law $$d_{hkl} = \frac{n\lambda}{2\sin\theta} \quad (3)$$

where n = 1 and λ for CuKα = 1.54439 A^o

Substituting n, λ, and θ into equation (3), we obtain

$$d_{101} = \frac{(1)(1.54439)}{(2)[\sin(25.44/2)]} = 3.507\ A^o$$

$$d_{200} = \frac{(1)(1.54439)}{(2)[\sin(48.20/2)]} = 1.891\ A^o$$

The d-spacing of (200) plane is used to determine a-cell parameter;

$$a = (2)(d_{200}) = (2)(1.891) = 3.782\ A^o \quad (4)$$

And c-cell parameter can be determined from Equation (5) below.

$$c = \left(-\frac{(d_{101})^2 (a)^2}{((d_{101})^2 - (a)^2)} \right)^{1/2} \tag{5}$$

$$= \left(-\frac{(3.507)^2 (3.782)^2}{((3.507)^2 - (3.782)^2)} \right)^{1/2} = 9.368 \text{ A}^{o}$$

The crystal volume of TiO_2 can be calculated from:

$$\text{Crystal volume of anatase } TiO_2 = (a)^2 (c) \tag{6}$$

$$= (3.782)^2 (9.368) = 133.995 \text{ A}^{o3}$$

Table F.2 Summary of lattice parameters and crystal volume from XRD analysis

Oxide samples	d_{101} (A^o)	d_{200} (A^o)	a-cell parameter (A^o)	c-cell parameter (A^o)	crystal volume (A^{o3})
Pure TiO_2	3.507	1.891	3.782	9.368	134.00
0.1% CeO_2/TiO_2	3.496	1.887	3.774	9.281	132.19
0.5% CeO_2/TiO_2	3.502	1.900	3.800	9.021	130.26
1% CeO_2/TiO_2	3.502	1.884	3.768	9.489	134.72
2% CeO_2/TiO_2	3.523	1.888	3.776	9.789	139.57
5% CeO_2/TiO_2	3.491	1.894	3.788	8.994	129.05
10% CeO_2/TiO_2	3.507	1.896	3.792	9.220	132.58

APPENDIX G

POSITION OF TITANIUM OXIDATION STATE

The content of each Ti oxidation state can determine from the component area (see Figure G.1) and each binding energy position is list in Table G.1

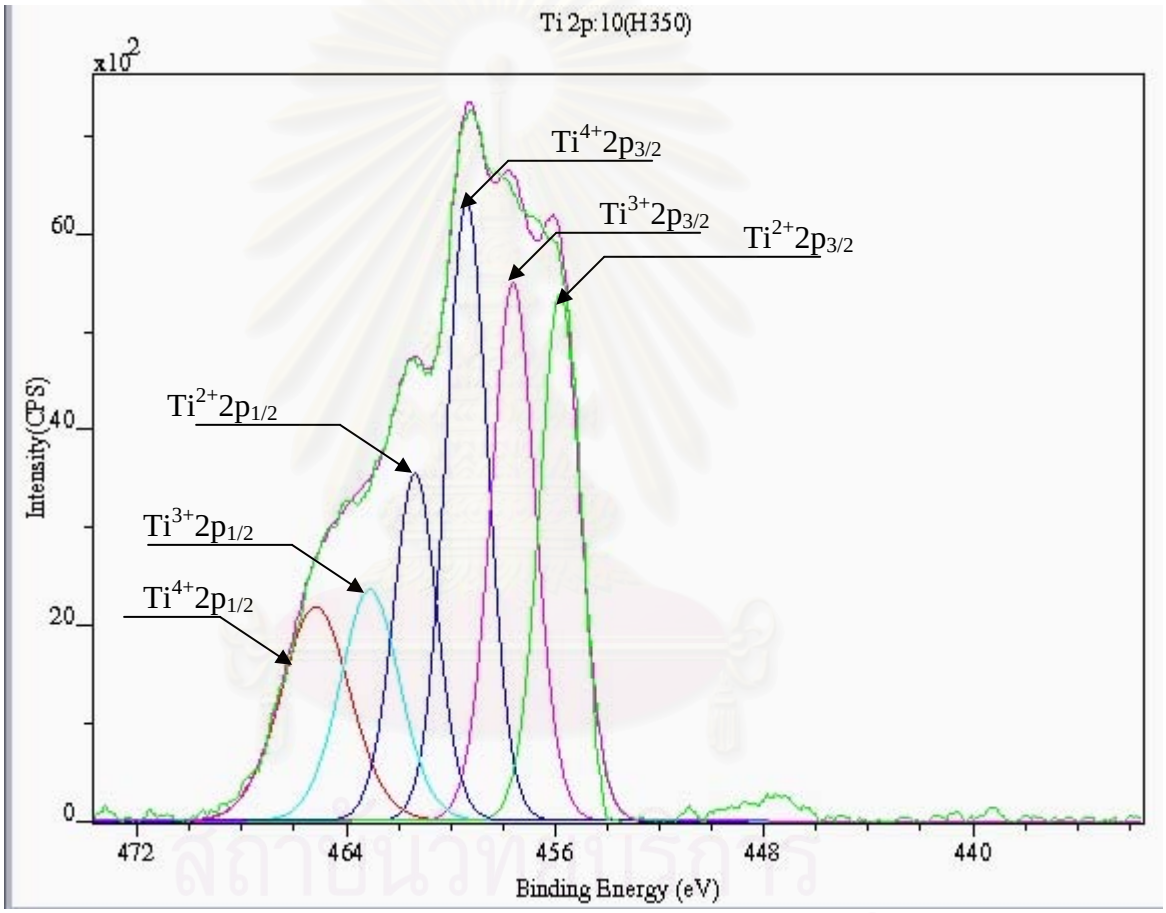

Figure G.1 The binding energy and area of each Ti oxidation state.

Table G.1 The list of binding energy position and reference of each element.

Element	Binding energy	Component	References.
O 1s	528.300	TiO	P.Madhu Kumar, Thin Films,2000
O 1s	531.100	Ti_2O_3	P.Madhu Kumar, Thin Films,2000
O 1s	530.100	TiO_2	P.Madhu Kumar, Thin Films,2000
O 1s	532.300	$(OH)^-$	P.Madhu Kumar, Thin Films,2000
O 1s	529.400	$(OH)^-$	Henrik Jensen, Applied Surface, 2005
Ti 2p	455.900	TiO	P.Madhu Kumar, Thin Films,2000
Ti 2p	456.700	Ti_2O_3	P.Madhu Kumar, Thin Films,2000
Ti 2p	485.500	TiO_2	P.Madhu Kumar, Thin Films,2000
Ti 2p	464.200	TiO_2	Nicola J.Price, 1999
Ti 2p	458.500	TiO_2	Nicola J.Price, 1999
Ti 2p	461.700	Ti_2O_3	Nicola J.Price, 1999
Ti 2p	456.100	Ti_2O3	Nicola J.Price, 1999
Ti 2p	464.280	TiO_2	Henrik Jensen, Applied Surface, 2005
Ti 2p	458.500	TiO_2	Henrik Jensen, Applied Surface, 2005
C 1s	288.400	C=C	Henrik Jensen, Applied Surface, 2005
C 1s	285.000	C-O (ref.)	Henrik Jensen, Applied Surface, 2005
C 1s	284.300	C-C	Henrik Jensen, Applied Surface, 2005

VITA

Mr. Seubsakul Pokasem was born on October 2, 1982 in Phichit province, Thailand. He received the Bachelor Degree of Chemical Engineering from Faculty of Engineering, King's Mongkut Institute of Technology North Bangkok, in 2003. He persued his Master's study at Chulalongkorn University in June, 2004.